




Electronic instabilities of kagome metals: Saddle points and Landau theoryTakamori Park ¹, Mengxing Ye ², and Leon Balents ^{2,3}¹*Department of Physics, University of California, Santa Barbara, California 93106-9530, USA*²*Kavli Institute for Theoretical Physics, University of California, Santa Barbara, California 93106-4030, USA*³*Canadian Institute for Advanced Research, 661 University Ave., Toronto, Ontario, Canada M5G 1M1*

(Received 17 April 2021; accepted 7 July 2021; published 22 July 2021)

We study electronic instabilities of a kagome metal with a Fermi energy close to saddle points at the hexagonal Brillouin zone face centers. Using parquet renormalization group, we determine the leading and subleading instabilities, finding superconducting, charge, orbital moment, and spin density waves. We then derive and use Landau theory to discuss how different primary density wave orders give rise to charge density wave modulations, as seen in the AV_3Sb_5 family, with $A = K, Rb, Cs$. The results provide strong constraints on the mechanism of charge ordering and how it can be further refined from existing and future experiments.

DOI: [10.1103/PhysRevB.104.035142](https://doi.org/10.1103/PhysRevB.104.035142)**I. INTRODUCTION**

Two-dimensional (2D) correlated metals based on transition metal ions are a classic subject for many-body physics [1,2], displaying diverse electronic phenomena such as unconventional superconductivity [3–5], charge and spin order [6,7], nematicity [8,9], strange metallic behavior [10–12], and more. These topics have been most heavily investigated in theory and experiment in structures based on square lattices in the cuprates [4,13] and Fe superconductors [3,14,15]. Correlated metals with hexagonal and triangular symmetry are much less common, with the best-known example being the triangular lattice cobaltates [16,17], which however are complicated by Na vacancy ordering and water intercalation [18].

Recently, a new class of kagome metals, with chemical formula AV_3Sb_5 , where $A = K, Rb, \text{ or } Cs$, have emerged as an exciting realization of quasi-2D correlated metals with hexagonal symmetry [19]. These materials have been shown to display several electronic orders setting in through thermodynamic phase transitions: multicomponent (“3Q”) hexagonal charge density wave (CDW) order below a $T_c \approx 90$ K [20–27], and superconductivity with critical temperature of 2.5 K or smaller [20,21,28–35], and some indications of nematicity and one-dimensional charge order in the normal and superconducting states [21,31,36]. Other experiments show a strong anomalous Hall effect [37,38], suggesting possible topological physics. Furthermore, density functional calculations identified CsV_3Sb_5 as a \mathbb{Z}_2 topological metal [39]. Angle-resolved photoemission studies show these materials to be multiband systems with several Fermi surface components [39], including approximately nested components and a Fermi energy that is close to multiple saddle points of the dispersion, in agreement with density functional theory [39,40]. Furthermore, strong momentum-dependent charge gaps near the saddle-point momenta were observed below the CDW transition temperature [41,42].

Many of these ingredients bring to mind a storied idea of electronic instabilities enhanced by van Hove singularities near saddle points. This mechanism figured heavily in early theoretical treatments of the cuprates [43–45], and references therein]. In a two-dimensional system, the divergence of the density of states generates enhanced scattering amongst electrons near the saddle points of the bands, which may drive not only superconducting but also other charge and spin instabilities. The same idea emerged recently in the context of doped graphene [46–48], and has been applied to the theory of magic-angle graphene bilayers [49–53]. The observations in AV_3Sb_5 suggest another application. Notably, the observed period of charge order in AV_3Sb_5 within the two-dimensional kagome plane is precisely that expected from scattering amongst the saddle points located at the hexagonal Brillouin zone face centers (denoted as M).

While the saddle-point model on a 2D hexagonal lattice has been studied extensively in the literature [46–49], its application to a coherent understanding of the electronic instabilities revealed in multiple experiments remains to be understood. First, the renormalization group studies from repulsive interactions [46,49] suggest leading spin density wave, superconductivity, and orbital moment instabilities, rather than the charge density wave order which is observed. Therefore, it is natural to expect that the lattice plays some role, and thus it is important to understand the combined effect of electron-phonon and electron correlation. Second, the strong anomalous Hall effect observed below the charge density wave critical temperature suggests time-reversal symmetry-breaking order may develop below T_c . It would be desirable to understand the interplay between time-reversal symmetric and broken CDW order. Third, in addition to the 2×2 charge density wave within the 2D layer, STM and x-ray studies also observed modulation in the z direction, i.e., $k_z \neq 0$, in RbV_3Sb_5 and CsV_3Sb_5 . The three-dimensional alignment of 2D charge density waves has not yet been studied theoretically.

In this paper, we explore the electronic instabilities due to interactions amongst electrons near the saddle points with hexagonal symmetry. We apply the parquet renormalization group scheme [54–57] to determine all the primary and secondary instabilities, generalizing prior work [46,49]. We further use mean field theory to study different possible emergent density wave states, which include not only a conventional charge density wave, but also spin and orbital moment density waves. We investigate how they relate to the observed charge density wave measured in AV_3Sb_5 . Through this analysis, we provide constraints on the interpretation of experimental observations, and suggestions for future theoretical and experimental studies.

The rest of this paper is structured as follows: In Sec. II, we construct a low-energy continuum model by taking patches around the saddle-point momenta \mathbf{M} and identify its connection to the real-space tight-binding model. In Sec. III, we generalize the parquet renormalization group formulation, and discuss all stable fixed points within the patch model. In Sec. IV, we analyze the mean field theory for each fixed-point solution. This includes a Landau theory analysis of the conventional charge density wave (Sec. IV B) as well as an analysis of other leading instabilities, i.e., the orbital moment density wave (Sec. IV C) and spin density wave (Sec. IV D), and their interplay with the conventional charge density wave. In Sec. V, we discuss the implications of the results obtained in Sec. IV to experimental observations. The real-space patterns on the kagome lattice are shown in Sec. V A. To understand the three-dimensional 3Q CDW order with $k_z \neq 0$, we study the effects of weak interlayer coupling and discuss the allowed k_z for both conventional CDW and orbital moment density wave orders. The experimentally observed anisotropic CDW order can also be explained within this picture. In Sec. V C, we discuss the critical behavior for different types of charge order instabilities. The staggered and uniform orbital moment is estimated in Sec. V D. The possibility of a magnetic field-induced mixture of conventional CDW and orbital moment is also briefly discussed there. Lastly, a summary of our work and discussions on the theoretical and experimental implications are presented in Sec. VI.

II. MODEL

In this section, we introduce a simple model to study the electronic behavior in AV_3Sb_5 . As explained in the Introduction, STM and x-ray scattering measurements show a 2×2 CDW order with wave vector $\mathbf{Q}_\alpha = \mathbf{Q}_{\text{Bragg}}/2$ [20–22,24]. These wave vectors are equivalent to the momenta that connect the three \mathbf{M}_α points in the hexagonal Brillouin zone as shown in Fig. 1(b). In addition, DFT calculations show that the band structure has saddle points at the \mathbf{M}_α points near the Fermi level as shown in Fig. 2 for CsV_3Sb_5 . In two-dimensional systems, a saddle point is a van Hove singularity with a logarithmically diverging density of states. Based on these two observations, we assume that the collective electronic behavior in AV_3Sb_5 is determined by the saddle points located at the \mathbf{M}_α points and the interactions between them.

From these considerations, we construct a noninteracting low-energy continuum model by taking patches around the \mathbf{M}_α points in the Brillouin zone with cutoff radius Λ . The

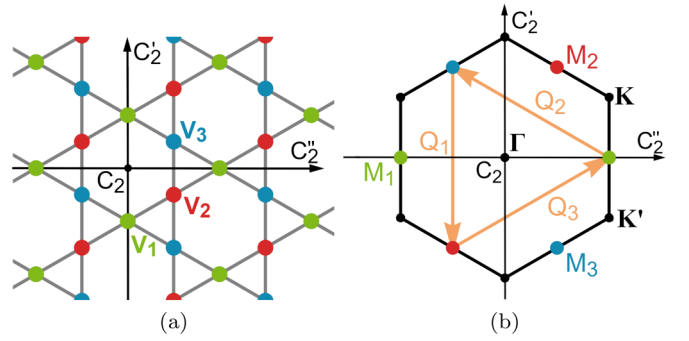


FIG. 1. (a) Vanadium kagome lattice structure in AV_3Sb_5 . The actual lattice structure has a Sb atom in the center of the hexagonal faces, but they are not shown here since our work is only focused on the electronic behavior of vanadium. The space group of the full lattice is $P6/mmm$. (b) Hexagonal Brillouin zone of AV_3Sb_5 . There are three distinct \mathbf{M} points along the Brillouin zone boundaries. The \mathbf{M}_α points in the Brillouin zone are connected by three nesting vectors $\{\mathbf{Q}_\alpha\}$. The nesting vectors satisfy $\mathbf{Q}_\alpha \equiv -\mathbf{Q}_\alpha$ up to a reciprocal lattice vector.

Hamiltonian of such a model is

$$H_0 = \sum_{\alpha} \sum_{|\mathbf{q}| < \Lambda} c_{\alpha\mathbf{q}}^{\dagger} [\varepsilon_{\alpha}(\mathbf{q}) - \mu] c_{\alpha\mathbf{q}}, \quad (1)$$

where α, β are patch indices, \mathbf{q} is the momentum measured from \mathbf{M}_α , $\varepsilon_{\alpha}(\mathbf{q})$ is the saddle-point dispersion sitting at \mathbf{M}_α , and μ is the chemical potential measured away from the saddle point. Up to quadratic order in \mathbf{q} , the saddle-point dispersions take the general form

$$\begin{aligned} \varepsilon_1(\mathbf{q}) &= aq_x^2 - bq_y^2, \\ \varepsilon_2(\mathbf{q}) &= \frac{a-3b}{4}q_x^2 + \frac{\sqrt{3}(a+b)}{2}q_xq_y + \frac{3a-b}{4}q_y^2, \\ \varepsilon_3(\mathbf{q}) &= \frac{a-3b}{4}q_x^2 - \frac{\sqrt{3}(a+b)}{2}q_xq_y + \frac{3a-b}{4}q_y^2, \end{aligned} \quad (2)$$

where $\mathbf{q} = (q_x, q_y)$. The parameters a, b that determine the shape of the saddle point must have the same sign $ab > 0$.

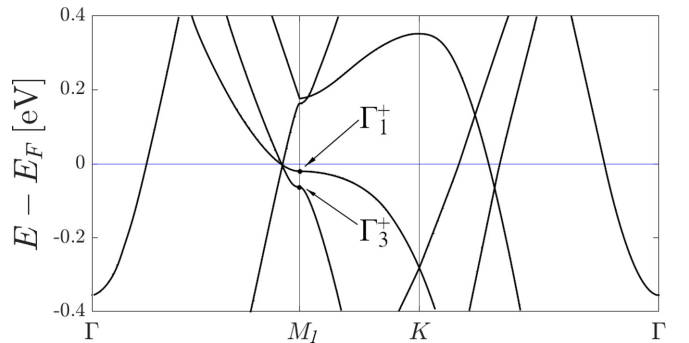


FIG. 2. Band structure of CsV_3Sb_5 calculated using DFT without spin-orbit coupling [58]. The Fermi energy is set to 6.81 eV. Γ_1^+, Γ_3^+ are the irreducible representations of the two saddle-point bands nearest the Fermi energy at \mathbf{M}_1 . The little cogroup at \mathbf{M}_1 is D_{2h} , and the orientation of the symmetry axes C_2, C_2', C_2'' is shown in Fig. 1. We use the notation found in Ref. [59].

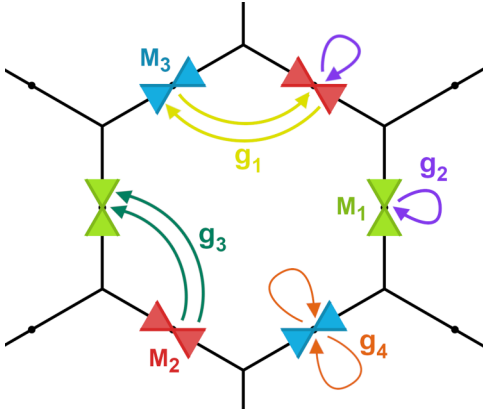


FIG. 3. All possible interactions in the patch model. The cones represent the saddle-point dispersion at each M_α and the arrows denote the scattering processes described by the interactions.

Note that the dispersion of the three patches is related by a threefold rotation. The condition for perfect nesting is given by $a/b = 3$, but in our work we will not necessarily impose this condition unless otherwise stated.

In general, there are four different cases of the form of the dispersion that we can consider: (i) $a, b > 0, a/b > 1$, (ii) $a, b > 0, a/b < 1$, (iii) $a, b < 0, a/b > 1$, and (iv) $a, b < 0, a/b < 1$. These cases can be all be mapped to case (i) by using two transformations. First, rotating the coordinates by $\pi/2$ takes cases (iii), (iv) to cases (ii), (i), respectively. Second, a particle-hole transformation combined with the same $\pi/2$ rotation maps case (ii) to case (i) (changing the sign of μ). Hence, we only need to consider case (i). Note that the latter particle-hole-like transformation becomes a symmetry when $a = b$ and $\mu = 0$.

Next, we introduce interactions to the continuum model by listing all possible electron-electron interactions between the fermions in the three patches. There are four such interactions,

$$\begin{aligned}
 H_1 = \frac{1}{2\mathcal{N}} \sum'_{|q_1|, \dots, |q_4| < \Lambda} & \left[\sum_{\alpha \neq \beta} (g_1 c_{\alpha q_1 \sigma}^\dagger c_{\beta q_2 \sigma'}^\dagger c_{\alpha q_3 \sigma'} c_{\beta q_4 \sigma} \right. \\
 & + g_2 c_{\alpha q_1 \sigma}^\dagger c_{\beta q_2 \sigma'}^\dagger c_{\beta q_3 \sigma'} c_{\alpha q_4 \sigma} \\
 & + g_3 c_{\alpha q_1 \sigma}^\dagger c_{\alpha q_2 \sigma'}^\dagger c_{\beta q_3 \sigma'} c_{\beta q_4 \sigma}) \\
 & \left. + \sum_{\alpha} g_4 c_{\alpha q_1 \sigma}^\dagger c_{\alpha q_2 \sigma'}^\dagger c_{\alpha q_3 \sigma'} c_{\alpha q_4 \sigma} \right], \quad (3)
 \end{aligned}$$

where $\sum'_{|q_1|, \dots, |q_4| < \Lambda} \equiv \sum_{|q_1|, \dots, |q_4| < \Lambda} \delta_{q_1+q_2, q_3+q_4}$, \mathcal{N} is the number of unit cells in the system, and g_i are the interactions that are defined to be intrinsic and have units of energy. As seen in Fig. 3, the g_1, g_2, g_3, g_4 interactions represent interpatch exchange, interpatch density-density, umklapp, and intrapatch density-density scattering processes, respectively. The values of g_i at energy scale Λ may be obtained from the screened Coulomb interaction [46].

The patch model introduced here has been used in previous works to study the interaction and competition between different instabilities in the Hubbard model and doped graphene [46,60]. An important thing to note is that the continuum

model defined above does not include details on the underlying structure of the lattice and the global band structure. We supplement the results of our model with the symmetry information provided by the DFT results for CsV_3Sb_5 shown in Fig. 2 [58]. This gives a one-to-one correspondence between Brillouin zone patches M_α and the vanadium sites V_α (see Appendix A). A minimal tight-binding model on the kagome lattice can be readily obtained from this correspondence to faithfully describe the saddle-point fermions (see Sec. VA2 for more discussions).

III. RENORMALIZATION GROUP ANALYSIS

While all four interactions g_1, g_2, g_3 , and g_4 are marginal at tree level, they acquire leading double-logarithmic corrections from particle-particle fluctuations at zero momentum [$\Pi_{\text{pp}}(0)$] and particle-hole fluctuations at momentum transfer M_α [$\Pi_{\text{ph}}(M_\alpha)$] at the one-loop level and so can become marginally relevant. To study the evolution of g_i at energy E as the fermion fluctuations from cutoff energy $\Lambda_{\text{RG}} \sim t\Lambda^2$ to E are integrated out, we perform a parquet renormalization group (pRG) analysis. Following Ref. [46], the pRG equations for g_i are

$$\begin{aligned}
 \frac{dg_1}{dy} &= 2d_1 g_1 (g_2 - g_1), \\
 \frac{dg_2}{dy} &= d_1 (g_2^2 + g_3^2), \\
 \frac{dg_3}{dy} &= -g_3^2 - 2g_3 g_4 + 2d_1 g_3 (2g_2 - g_1), \\
 \frac{dg_4}{dy} &= -2g_3^2 - g_4^2, \quad (4)
 \end{aligned}$$

where $y = \Pi_{\text{pp}}(0, E) \sim \ln^2(\Lambda_{\text{RG}}/E)$ is the RG scale and $d_1(y) = d\Pi_{\text{ph}}(M_\alpha)/dy$ depends on the Fermi surface nesting, which satisfies $0 < d_1(y) \leq \frac{1}{2}$. For perfect nesting, $d_1(y) = \frac{1}{2}$ and is independent of the RG scale. Away from perfect nesting, $d_1(y)$ depends on the RG scale and is bounded $0 < d_1(y) < \frac{1}{2}$. It has been confirmed numerically that the nesting condition does not qualitatively change the fixed-point solutions and leading density wave instabilities, so for concreteness, we will consider the perfect nesting case hereafter, i.e., $d_1 \equiv \frac{1}{2}$.

The RG equations, having entirely quadratic β functions (the right-hand sides of the pRG equations), do not have any nontrivial controlled fixed points in the usual sense. Rather, they describe flows in the vicinity of the free fixed point: since the RG equations are perturbative, they are strictly valid only within some sphere of small radius of the origin in g space. Within certain domains of this space, the flows will be unstable, i.e., they will exit the sphere of control, which indicates an instability towards a new regime, and most likely an ordered state. Within the unstable regions of phase space, RG flows that begin very close to the origin tend to converge toward particular unstable trajectories which act as attractors, and are typically straight ‘‘rays’’ [61,62]. Below we follow previous works that reformulate these rays to appear as fixed points, by projecting the trajectories to a plane of constant value of one of the parameters. The stable ‘‘fixed rays’’ are

TABLE I. List of all bilinear order parameters (OPs) in the patch model. σ are the Pauli matrices in spin space, and $\sum_q \equiv \sum_{|q|<\Lambda} \cdot D_{xy}, D_{x^2-y^2}$ are matrices in the patch space defined as $D_{xy} = \sqrt{1/2} \text{diag}(0, 1, -1)$ and $D_{x^2-y^2} = \sqrt{2/3} \text{diag}(1, -1/2, -1/2)$, and $c_{q\sigma} = (c_{1q\sigma}, c_{2q\sigma}, c_{3q\sigma})$.

OP	Definition	Interaction strength (G)
rCDW	$N_\alpha = G_{\text{rCDW}} \frac{ c_{\alpha\beta\gamma} }{2N} \sum_q \langle c_{\beta q}^\dagger c_{\gamma q} \rangle$	$-2g_1 + g_2 - g_3$
iCDW	$\phi_\alpha = G_{\text{iCDW}} \frac{c_{\alpha\beta\gamma}}{2iN} \sum_q \langle c_{\beta q}^\dagger c_{\gamma q} \rangle$	$-2g_1 + g_2 + g_3$
rSDW	$S_\alpha = G_{\text{rSDW}} \frac{ c_{\alpha\beta\gamma} }{2N} \sum_q \langle c_{\beta q}^\dagger \frac{\sigma}{2} c_{\gamma q} \rangle$	$g_2 + g_3$
iSDW	$\psi_\alpha = G_{\text{iSDW}} \frac{c_{\alpha\beta\gamma}}{2iN} \sum_q \langle c_{\beta q}^\dagger \frac{\sigma}{2} c_{\gamma q} \rangle$	$g_2 - g_3$
sSC	$\Delta_s = G_{\text{sSC}} \frac{1}{\sqrt{3}N} \sum_q \langle c_{\alpha q\downarrow} c_{\alpha-q\uparrow} \rangle$	$-2g_3 - g_4$
	$\Delta_{xy} = G_{\text{dSC}} \frac{1}{N} \times \sum_q \langle c_{q\downarrow} D_{xy} c_{-q\uparrow} \rangle$	
dSC	$\Delta_{x^2-y^2} = G_{\text{dSC}} \frac{1}{N} \times \sum_q \langle c_{q\downarrow} D_{x^2-y^2} c_{-q\uparrow} \rangle$	$g_3 - g_4$

expected to describe the asymptotic limit of arbitrarily weak but nonzero bare interaction, such that convergence to these rays is nearly perfect before the sphere of control is exited. One should keep in mind that when the bare interactions are small but not arbitrarily so, the deviations from these rays become important, and the physics will be less universal and controlled more by the actual values of the interactions, but the RG equations can still be employed.

Before considering the stable fixed rays, we note a few features of these equations. The β functions for g_1 and g_3 contain an overall factor of g_1 and g_3 , respectively. This follows from symmetry: all terms except g_1 conserve spin at each saddle point separately, and all terms except g_3 conserve the number of electrons at each saddle point separately. The conserving interactions cannot generate a nonconserving one. As a result, the sign of g_1 and g_3 remains fixed throughout the RG evolution. One also notes that the $dg_2/dy > 0$ and $dg_4/dy < 0$ under the RG. Thus, an initially positive g_2 must remain positive, and an initially negative g_4 remains negative.

To understand the physical meaning of the g_i , it is useful to define interactions that parametrize particular channels of ordering, e.g., they appear in the mean field treatment below in Sec. IV. They were previously defined in Refs. [46,49]. Here, we consider the interactions in the d -wave superconductivity ($G_{\text{dSC}} = g_3 - g_4$), s -wave superconductivity ($G_{\text{sSC}} = -2g_3 - g_4$), real charge density ($G_{\text{rCDW}} = -2g_1 + g_2 - g_3$), orbital moment density ($G_{\text{iCDW}} = -2g_1 + g_2 + g_3$),¹ real spin density ($G_{\text{rSDW}} = g_2 + g_3$), spin-flux order ($G_{\text{iSDW}} = g_2 - g_3$)

¹Here, iCDW stands for ‘‘imaginary charge density wave.’’ However, note that the latter does not necessarily mean that the charge instability must break time-reversal symmetry for a generic wave vector. But at wave vector $\mathbf{M} = -\mathbf{M}$ up to a reciprocal lattice vector, imaginary charge density must break time-reversal symmetry, and

channels. The interactions G_a are defined such that the a instability develops only when $G_a > 0$. The interactions G_a and the definitions of their corresponding order parameters are summarized in Table I.

From the previous discussion, we can see a few features clearly. Real and imaginary parts of the CDW and SDW order parameters (OPs) are degenerate if $g_3 = 0$. This is because the umklapp interaction is the only one transferring charge between saddle points, so that in its absence there is a separate U(1) charge rotation for each valley. Similarly, the corresponding real and imaginary parts of the CDW and SDW orders are degenerate when $g_1 = 0$. This is because only g_1 violates separate spin conservation at each saddle, so that when $g_1 = 0$, independent SU(2) rotations may be made for each flavor, which mixes CDW and SDW orders. Thus, we see that the sign of g_3 decides between real and imaginary CDW/SDW, while the sign of g_1 decides between CDW and SDW order.

To proceed further, we determine the fixed rays and the pRG flow trajectory near them. We rewrite interactions as $g_i = \gamma_i \mathbf{g}$, and choose \mathbf{g} as one of the interactions, which diverges as $\mathbf{g} \sim \frac{1}{y_c - y}$ along the fixed trajectory (as we verify afterwards). A proper identification of \mathbf{g} ensures that γ_i tends to a constant value γ_i^* along the fixed trajectory, and $\gamma_i^* = 0$ implies that the interaction g_i either flows to zero or diverges slower than $\frac{1}{y_c - y}$. We call it a fixed point hereafter. The solutions to γ_i^* can be obtained by solving a set of algebraic equations $\tilde{\beta}_i(\{\gamma\}) = 0$ for $i = 1, 2, 3, 4$, where

$$\tilde{\beta}_i(\{\gamma\}) = \dot{\gamma}_i = \frac{1}{\mathbf{g}} (\dot{g}_i - \gamma_i \dot{\mathbf{g}}). \quad (5)$$

When substituting Eqs. (4) into the right-hand side of Eq. (5), we replace $d_1(y)$ with its value at y_c , $d_1(y_c)$, and treat $d_1(y_c)$ as a tunable parameter used to introduce information on Fermi surface nesting. This is why d_1 is referred to as the ‘‘nesting parameter.’’ Among the solutions of Eq. (5), only the stable fixed-point solutions are of physical interest, as they do not flow away under small perturbations. To examine the stability of a fixed-point solution, we define a matrix \mathbf{T} that is determined by the flow of $\tilde{\beta}_i$ at the fixed point, i.e., $T_{ij} = \partial \tilde{\beta}_i / \partial \gamma_j |_{\{\gamma^*\}}$. The RG fixed point is stable only when all the eigenvalues of \mathbf{T} are nonpositive.

In addition to identifying the leading instabilities, the subleading ones are also considered here for three reasons. *First*, as discussed above, when the interaction strengths are not truly infinitesimal, flow to the unstable regime may occur before the fixed ray is reached. This may occur when bare couplings are small but not too close to a fixed ray, and deviate from it in a particular direction favoring a subleading instability. *Second*, the flow may be also cut off by imperfect nesting and/or a nonzero chemical potential (i.e., doping from the saddle point). These effects limit the convergence to the fixed ray, and at that point a different instability might dominate. *Third*, a secondary instability may develop at a lower temperature, even if the primary one occurs first. To account

correspond to orbital moment density wave. For similar reasoning, we use iSDW for spin-flux order.

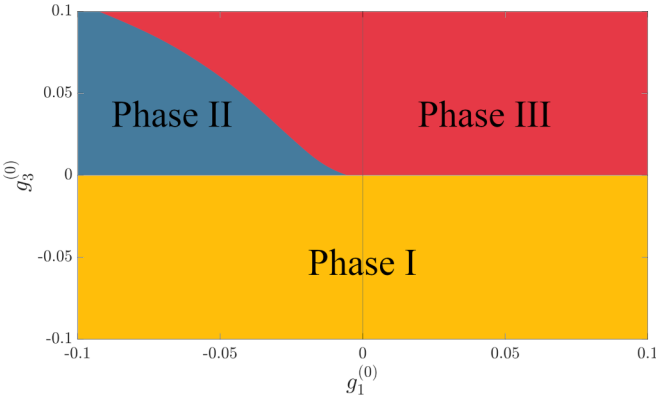


FIG. 4. RG phase diagram for $g_2^{(0)} > 0$. The leading instabilities of each phase under RG are as follows: Phase I: sSC, rCDW, iSDW; Phase II: iCDW and rCDW; and Phase III: dSC, rSDW, iCDW. The phase diagram was calculated assuming $d_1 = 1/2$, $g_2^{(0)} = 0.1$, $g_4^{(0)} = 0.3$.

for those possibilities, which depend upon the microscopic details, we will list the leading two instabilities at the RG fixed points.

To summarize, we list all the stable fixed-point solutions for both repulsive and attractive bare interactions. In addition, we discuss an interesting semistable fixed-point solution with only one weak unstable direction flowing out of the fixed point.

When $g_2^{(0)} > 0$, there are three (semi)stable fixed points, which we take the liberty of denoting “phases” I, II, III: this is an abuse of terminology since these solutions really describe unstable rays in the full phase space, which may not correspond to a unique phase. As $g_2(y)$ must diverge as $\sim \frac{1}{y_c - y}$, we choose $\mathbf{g}(y) = g_2(y) = \frac{1}{d_1(1+\gamma_3^2)(y_c - y)}$.

I. When $g_3^{(0)} < 0$, g_3 flows to negative value at the stable RG fixed point, and we find $\gamma_1 = 0$, $\gamma_2 = 1$, $\gamma_3 \approx -6.1$, $\gamma_4 \approx -5.5$. The subleading divergence of g_1 goes as $g_1(y) \sim (y_c - y)^{-\frac{2}{1+\gamma_3^2}} \sim \frac{1}{(y_c - y)^{0.05}}$. Note that as the flow of g_1 is subleading here, the sign of $g_1^{(0)}$ is not qualitatively important to determine the fixed trajectory. The leading instabilities are $G_{\text{sSC}} = 17.6\mathbf{g}$, $G_{\text{rCDW}} = G_{\text{iSDW}} = 7.1\mathbf{g}$.

II. When $g_1^{(0)} < 0$, $g_3^{(0)} > 0$, and for large enough $|g_1^{(0)}|$, the system may flow to a semistable fixed point, where there is only one weak unstable direction in the four-dimensional parameter space defined by $\{g_1, g_2, g_3, g_4\}$. The fixed-point solution reads as $\gamma_1 \approx -46.7$, $\gamma_2 = 1$, $\gamma_3 \approx 9.7$, $\gamma_4 \approx -4.4$. The leading instabilities are $G_{\text{iCDW}} = 104.0\mathbf{g}$, $G_{\text{rCDW}} = 84.6\mathbf{g}$.

III. When $g_1^{(0)}, g_3^{(0)} > 0$, the stable RG fixed point has been discussed a lot in the literature [46]. The fixed-point solution gives $\gamma_1 = 0$, $\gamma_2 = 1$, $\gamma_3 \approx 5.6$, $\gamma_4 \approx -10.0$, where the subleading divergence of g_1 can be obtained as $g_1(y) \sim (y_c - y)^{-\frac{2}{1+\gamma_3^2}} \approx \frac{1}{(y_c - y)^{0.06}}$. The leading divergent instabilities are $G_{\text{dSC}} = 15.6\mathbf{g}$, $G_{\text{rSDW}} = G_{\text{iCDW}} = 6.6\mathbf{g}$.

In Fig. 4, the phase diagram in the space of $g_1^{(0)}, g_3^{(0)}$ for $g_2^{(0)} > 0$ is shown.

When $g_2^{(0)} < 0$, g_2 may instead flow to zero. We find in this way a fourth fixed ray, which we denote phase IV. It is de-

scribed by letting $\mathbf{g} = g_1(y) = -\frac{1}{2d_1(y_c - y)}$, and $\gamma_1 = 1$, $\gamma_2 = 0$, $\gamma_3 = 0$, $\gamma_4 = 0$. This solution requires $g_1^{(0)} < 0$, $g_4^{(0)} > 0$, and is only stable when $g_3^{(0)} > 0$. Moreover, $g_3(y)$ is also divergent and is only logarithmically smaller than g_1 . We find $g_3(y) = \frac{1}{y_c - y} (\ln \frac{1}{y_c - y})^{-1}$. The leading instabilities are $G_{\text{rCDW}} = G_{\text{iCDW}} = -2\mathbf{g} = \frac{1}{d_1(y_c - y)}$. The fixed-point solution indicates that the rCDW and iCDW orders are degenerate at the leading order, but they are split by a logarithmically subdominant effect due to $g_3 > 0$ weakly in favor of the iCDW, i.e., $G_{\text{iCDW}} > G_{\text{rCDW}}$.

In passing, we note that purely electronic interactions generally give repulsion for all couplings, i.e., $g_i^{(0)} > 0$ with $i = 1, 2, 3, 4$. However, other factors, such as orbital composition of the wave function near saddle points, and electron-phonon coupling, may contribute to attraction for certain $g_i^{(0)}$. In Appendix B, we consider the effect of electron-phonon coupling, and show that the renormalization to $g_i^{(0)}$ can be attractive for both $\delta g_1^{(0)}$ and $\delta g_3^{(0)}$ or only $\delta g_1^{(0)}$, depending upon the strength of the coupling and and phonon modes involved.

IV. MEAN FIELD THEORY

As shown in Sec. III, we found instabilities to superconducting, charge density wave (rCDW), orbital moment (iCDW), and spin density wave (SDW) states. In all three AV_3Sb_5 materials, experiments have observed charge density wave order (rCDW order) setting as the first instability of the symmetric state at a $T_c \sim 90$ K, and superconductivity only at much lower temperatures. Hence, in this section, we neglect superconductivity, and discuss the ways that the remaining instabilities may lead to the specific rCDW order observed experimentally in the AV_3Sb_5 materials. Notably, we find that rCDW order can be induced even if rCDW is not the primary order parameter. Hence, we study the formation of rCDWs both when the rCDW is and is not the primary instability, and discuss the differences in the resulting properties. We carry out the study using mean field theory.

The renormalization group analysis tells us that in phase I the rCDW is a leading instability. In Sec. IV B, we will study this case by calculating a mean field theory in the rCDW channel. In Sec. IV C, we consider a iCDW-rCDW coupled mean field theory, which is relevant to phases II and IV. Here we discuss how rCDW can be induced when the iCDW is the primary order parameter. Finally, in Sec. IV D, we consider the situation with a leading rSDW instability, relevant to phase III, and show how it may induce rCDW order.

A. Complex CDW free energy

We first obtain the Landau free energy including both rCDW and iCDW order parameters, defined as N_α, ϕ_α with $\alpha = 1, 2, 3$ labeling the interpatch momentum transfer \mathbf{Q}_α [see Fig. 1(b)], respectively. The patch-model interaction given in Eq. (3) can be rewritten in the form of a rCDW

interaction and an iCDW interaction:

$$H_{\text{rCDW}} = -\frac{\mathcal{N}G_{\text{rCDW}}}{2} \sum_{\alpha} \hat{\rho}_{\text{rC},\alpha} \hat{\rho}_{\text{rC},\alpha}, \quad (6)$$

$$H_{\text{iCDW}} = -\frac{\mathcal{N}G_{\text{iCDW}}}{2} \sum_{\alpha} \hat{\rho}_{\text{iC},\alpha} \hat{\rho}_{\text{iC},\alpha},$$

where $G_{\text{rCDW/iCDW}}$ is the rCDW/iCDW interaction strength defined in Sec. III and $\hat{\rho}_{\text{rC},\alpha} = \frac{|\epsilon_{\alpha\beta\gamma}|}{2\mathcal{N}} \sum_{|q|<\Lambda} c_{\beta q}^{\dagger} c_{\gamma q}$, $\hat{\rho}_{\text{iC},\alpha} = \frac{\epsilon_{\alpha\beta\gamma}}{2i\mathcal{N}} \sum_{|q|<\Lambda} c_{\beta q}^{\dagger} c_{\gamma q}$ is the rCDW and iCDW operators with momentum $\mathbf{Q}_{\alpha} = \mathbf{M}_{\beta} - \mathbf{M}_{\gamma}$. Using the Hubbard-Stratonovich transformation we decouple the interactions in the two channels and then integrate out the fermionic degrees of freedom. This gives us the free energy as a function of the rCDW and iCDW order parameters $N_1, N_2, N_3, \phi_1, \phi_2, \phi_3$:

$$F_{\text{CDW}} = \frac{\mathcal{N}}{2G_{\text{rCDW}}} \sum_{\alpha=1}^3 N_{\alpha}^2 + \frac{\mathcal{N}}{2G_{\text{iCDW}}} \sum_{\alpha=1}^3 \phi_{\alpha}^2 - (\text{Tr} \log \mathcal{G}^{-1}), \quad (7)$$

where \mathcal{G}^{-1} is defined as

$$\mathcal{G}^{-1}(i\omega_n, \mathbf{q}; \{N_{\alpha}, \phi_{\alpha}\}) = \begin{bmatrix} -i\omega_n + \varepsilon_1(\mathbf{q}) & -(N_3 - i\phi_3)/2 & -(N_2 + i\phi_2)/2 \\ -(N_3 + i\phi_3)/2 & -i\omega_n + \varepsilon_2(\mathbf{q}) & -(N_1 - i\phi_1)/2 \\ -(N_2 - i\phi_2)/2 & -(N_1 + i\phi_1)/2 & -i\omega_n + \varepsilon_3(\mathbf{q}) \end{bmatrix}. \quad (8)$$

Expanding the order-parameter fields in Eq. (8) perturbatively, the free energy in terms of the complex charge density order parameter $\Delta_{\alpha} = N_{\alpha} + i\phi_{\alpha} = |\Delta_{\alpha}|e^{i\theta_{\alpha}}$ is

$$f_{\text{CDW}} = \frac{r_N + r_{\phi}}{2} \sum_{\alpha} |\Delta_{\alpha}|^2 + \frac{r_N - r_{\phi}}{2} \sum_{\alpha} |\Delta_{\alpha}|^2 \cos 2\theta_{\alpha} + K_2 |\Delta_1| |\Delta_2| |\Delta_3| \cos(\theta_1 + \theta_2 + \theta_3) + K_4 \left(\sum_{\alpha} |\Delta_{\alpha}|^2 \right)^2 + (K_3 - 2K_4) \sum_{\alpha < \beta} |\Delta_{\alpha}|^2 |\Delta_{\beta}|^2 + O(\Delta^5). \quad (9)$$

Here, $r_N = \frac{1}{2G_{\text{rCDW}}} + K_1$, $r_{\phi} = \frac{1}{2G_{\text{iCDW}}} + K_1$, and K_1, \dots, K_4 are functions of temperature and chemical potential, that we will discuss in detail in Sec. IV B. For simplicity, we first consider the case $K_3 - 2K_4 < 0$, which favors 3Q CDW. The configuration of θ_{α} that minimizes the free energy depends on the sign of $r_N - r_{\phi}$:

(i) When $r_N < r_{\phi}$, i.e., $G_{\text{rCDW}} > G_{\text{iCDW}} > 0$, minimizing the second term requires $\theta_{\alpha} = n_{\alpha}\pi$, with $n_{\alpha} \in \mathbb{Z}$. By choosing the proper n_{α} , the minimization of cubic term can be readily achieved. For any $\theta_{\alpha} = n_{\alpha}\pi$, the iCDW order parameter must vanish, so the ground state only contains rCDW order.

(ii) When $r_N = r_{\phi}$, i.e., $G_{\text{rCDW}} = G_{\text{iCDW}}$, the second term vanishes, and the minimization of the cubic term gives a continuously degenerate ground-state manifold. To lift the degeneracy, other perturbations should be considered.

(iii) When $r_N > r_{\phi}$, i.e., $0 < G_{\text{rCDW}} < G_{\text{iCDW}}$, the second quadratic and cubic terms cannot be minimized simultaneously. As a result, $\theta_{\alpha} \neq n_{\alpha}\pi/2$, with $n_{\alpha} \in \mathbb{Z}$. This indicates that both N_{α} and ϕ_{α} are nonzero. To analyze the free energy

with iCDW as the leading instability, the iCDW-rCDW coupling must be considered.

Below, we discuss the above three scenarios and then the rSDW-rCDW coupling scenario.

B. rCDW mean field theory

At the RG fixed point corresponding to phase I ($g_3^{(0)} < 0$), the rCDW is the leading density wave instability. As argued above, it is enough to consider only the rCDW order parameters. The mean field free energy becomes

$$F_{\text{rCDW}} = \frac{\mathcal{N}}{2G_{\text{rCDW}}} \sum_{\alpha=1}^3 N_{\alpha}^2 - (\text{Tr} \log \mathcal{G}^{-1}), \quad (10)$$

where \mathcal{G}^{-1} is defined as

$$\mathcal{G}^{-1}(i\omega_n, \mathbf{q}; \{N_{\alpha}\}) = \begin{bmatrix} -i\omega_n + \varepsilon_1(\mathbf{q}) & -N_3/2 & -N_2/2 \\ -N_3/2 & -i\omega_n + \varepsilon_2(\mathbf{q}) & -N_1/2 \\ -N_2/2 & -N_1/2 & -i\omega_n + \varepsilon_3(\mathbf{q}) \end{bmatrix}. \quad (11)$$

As a function of N_{α} , the rCDW free energy has the symmetry of the tetrahedral point group T_d . This can be deduced by applying the symmetry operations of the full space group of the lattice, $P6/mmm$, to the definitions of the rCDW order parameter. Using our knowledge of this symmetry, we can determine what solutions of the free energy are possible. In the cases that are physically relevant, the solutions of the mean field theory belong in either the 3Q+, 3Q-, or 1Q rCDW configurations which are classes of rCDW states with directions:

$$\begin{aligned} 3\text{Q}+: & \{(111), (1\bar{1}\bar{1}), (\bar{1}\bar{1}1), (\bar{1}1\bar{1})\}, \\ 3\text{Q}-: & \{(\bar{1}\bar{1}\bar{1}), (\bar{1}11), (1\bar{1}1), (11\bar{1})\}, \\ 1\text{Q}: & \{(100), (\bar{1}00), (010), (0\bar{1}0), (001), (00\bar{1})\}. \end{aligned}$$

Indeed, by numerically solving the full free energy we will see that the solutions belong in either the 3Q± or 1Q rCDW classes. A detailed discussion is provided in Appendix C. The rCDW patterns of the 3Q± and 1Q states are shown in Fig. 7.

By assuming we are near the rCDW transition where the rCDW order parameters are sufficiently small, we can expand the free energy to fourth order in N_{α} . The resulting Landau theory is

$$f_{\text{rCDW}} = \left(\frac{1}{2G_{\text{rCDW}}} + K_1 \right) \sum_{\alpha} N_{\alpha}^2 + K_2 N_1 N_2 N_3 + K_4 \left(\sum_{\alpha} N_{\alpha}^2 \right)^2 + (K_3 - 2K_4) \sum_{\alpha < \beta} N_{\alpha}^2 N_{\beta}^2 + O(N^5), \quad (12)$$

where f_{rCDW} is the free-energy density. The definitions of the coefficients K_1, \dots, K_4 which are functions of chemical potential and temperature are given in Appendix D. The coefficients can be evaluated asymptotically in the limit $\mu, k_B T \ll t\Lambda^2$ and can also be found in Appendix D.

Figure 5 shows the temperature dependence of these coefficients when $\mu/t\Lambda^2 = 0.01$. Notice that the coefficients exhibit a change in behavior at the crossover temperature

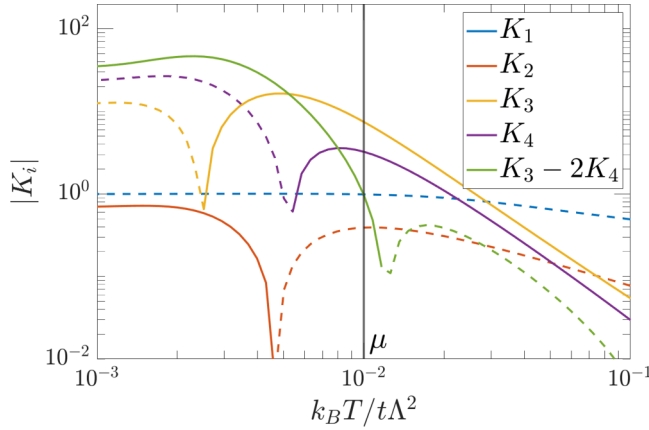


FIG. 5. Absolute value of the Landau theory coefficients K_1, \dots, K_4 evaluated at $\mu/t\Lambda^2 = 10^{-2}$ for the case of perfect nesting ($a = 9t/4$, $b = 3t/4$). Solid lines indicate positive values and dashed lines indicate negative values. K_2, K_3, K_4 change sign at $\mu/k_B T \sim 2.14, 4.05, 1.91$, respectively.

$k_B T \sim \mu$. In addition, the K_2, K_3, K_4 coefficients change sign near the crossover temperature. When the quartic coefficients become negative, the Landau theory expression given by Eq. (12) becomes unstable, but in those regions stability can be restored by including sixth-order terms to the free energy.

Equation (12) has a third-order term K_2 that couples all three rCDW order parameters. This is allowed by symmetry since this term is even under time-reversal symmetry and the sum of the three nesting wave vectors satisfies $\sum_{\alpha} \mathbf{Q}_{\alpha} \equiv 0$. This term introduces a preference for 3Q+ or 3Q- rCDW states depending on the sign of K_2 . On the other hand, when $K_3 - 2K_4 > 0$, the fourth-order term sets a preference for 1Q rCDW states. When $K_3 - 2K_4 < 0$, this fourth-order term prefers the 3Q± states equally.

When $a/b = 3$, Fig. 5 shows that $K_2 < 0$ when $\mu/k_B T \lesssim 2.14$ in the asymptotic limit. In addition, $K_3 - 2K_4 < 0$ for $\mu \ll k_B T$. Hence, in this region, all terms in the rCDW Landau theory prefer the 3Q+ rCDW state. The transition to the 3Q+ rCDW state must be a first-order transition because the free energy can become negative before the second-order term vanishes due to the third-order term. One thing to note is that the rCDW order parameter is not necessarily small near the first-order rCDW transition, so the results of the Landau theory must be treated with caution. We can avoid this issue by numerically solving the full free energy.

The full free energy defined in Eqs. (10) and (11) has four tunable parameters: temperature T , chemical potential μ , the rCDW interaction strength G_{rCDW} , and the nesting ratio a/b . As explained in Sec. II, we only need to consider the case $a, b > 0$. Given this condition, we can introduce a convenient reparametrization

$$\begin{aligned} a &= \frac{\delta + \sqrt{3 + \delta^2}}{\sqrt{3}} t, \\ b &= \frac{-\delta + \sqrt{3 + \delta^2}}{\sqrt{3}} t, \end{aligned} \quad (13)$$

where $t > 0$ and $\delta \in \mathbb{R}$. We see that t represents the bandwidth of the saddle-point band and δ represents the degree

of nesting. Under this parametrization, $a/b \geq 1$ for $\delta \geq 0$ and $a/b < 1$ for $\delta < 0$. In particular, $a/b = 3$ (perfect nesting) for $\delta = 1$.

For different values of G_{rCDW} and δ , we numerically generated a phase diagram in the T - μ plane. The results shown in Fig. 6 are representative samples of the entire parameter space where the continuum model holds: $k_B T, \mu, G_{\text{rCDW}} \ll t\Lambda^2$. The free energy was cast in a form that is independent of the cutoff momentum Λ , so the phase diagrams are independent of Λ . We see that when the system is doped to the saddle point ($\mu = 0$) or below it, only the 3Q+ rCDW forms. As you dope the system above the saddle point, 1Q and/or 3Q- rCDW regions can emerge. In addition, for $\delta = 1.6$, the 1Q rCDW region is small and vanishes for sufficiently small G_{rCDW} as seen in Figs. 6(c) and 6(f). Similarly, at perfect nesting and more generally $\delta \sim 1$, the 3Q- rCDW region vanishes for sufficiently small G_{rCDW} as seen in Fig. 6(b). Clearly, the 3Q+ rCDW region is largest in all phase diagrams which is consistent with the Landau theory discussed above.

C. iCDW-rCDW mean field theory

Now, we consider how a fundamental iCDW order can induce subsidiary rCDW order. To do so, we consider a iCDW-rCDW coupled mean field theory. We are particularly interested in the regime, motivated by the RG results for phases II and IV, in which iCDW and rCDW are close in energy and can compete.

It is convenient to express Eq. (9) in terms N_{α} and ϕ_{α} :

$$\begin{aligned} f_{\text{CDW}} &= r_{\phi} \sum_{\alpha=1}^3 \phi_{\alpha}^2 + r_N \sum_{\alpha=1}^3 N_{\alpha}^2 \\ &+ K_2 (N_1 N_2 N_3 - \phi_2 \phi_3 N_1 - \phi_1 \phi_3 N_2 - \phi_2 \phi_1 N_3) \\ &+ K_4 \left(\sum_{\alpha=1}^3 \phi_{\alpha}^2 + N_{\alpha}^2 \right)^2 + (K_3 - 2K_4) \\ &\times \sum_{\alpha < \beta} (\phi_{\alpha}^2 + N_{\alpha}^2)(\phi_{\beta}^2 + N_{\beta}^2) + O(\phi^6, N^5). \end{aligned} \quad (14)$$

Recall that $r_{\phi} = (\frac{1}{2G_{\text{iCDW}}} + K_1)$, $r_N = (\frac{1}{2G_{\text{rCDW}}} + K_1)$. We assume $G_{\text{iCDW}} > G_{\text{rCDW}} > 0$, so that iCDW is the leading instability. Note that time-reversal symmetry forbids the term cubic in ϕ , i.e., $\phi_1 \phi_2 \phi_3$. As a result, the order-parameter manifold for ϕ_{α} alone has cubic symmetry O_h . In addition, the 3Q± classes which were distinct for the case of rCDW are now related under time-reversal symmetry and part of the larger 3Q class which is defined as the union of the 3Q± classes. Close to and below the transition temperature for iCDW, the iCDW-rCDW coupling can be treated as a perturbation.

First, we consider the iCDW Landau theory. The order-parameter manifold for ϕ_{α} is determined by quartic terms proportional to K_3 and K_4 . The first term $K_4 (\sum_{\alpha=1}^3 \phi_{\alpha}^2)^2$ is positive definite and isotropic, so the selection of the ground-state configuration is determined by the term $(K_3 - 2K_4) \sum_{\alpha < \beta} \phi_{\alpha}^2 \phi_{\beta}^2$. Specifically, (i) when $K_3 > 2K_4$, the iCDW state is favored, (ii) when $K_3 = 2K_4$, the ϕ_{α} ground-state configuration is degenerate at quartic order, and requires higher-order terms to break the degeneracy, (iii) when $K_3 <$

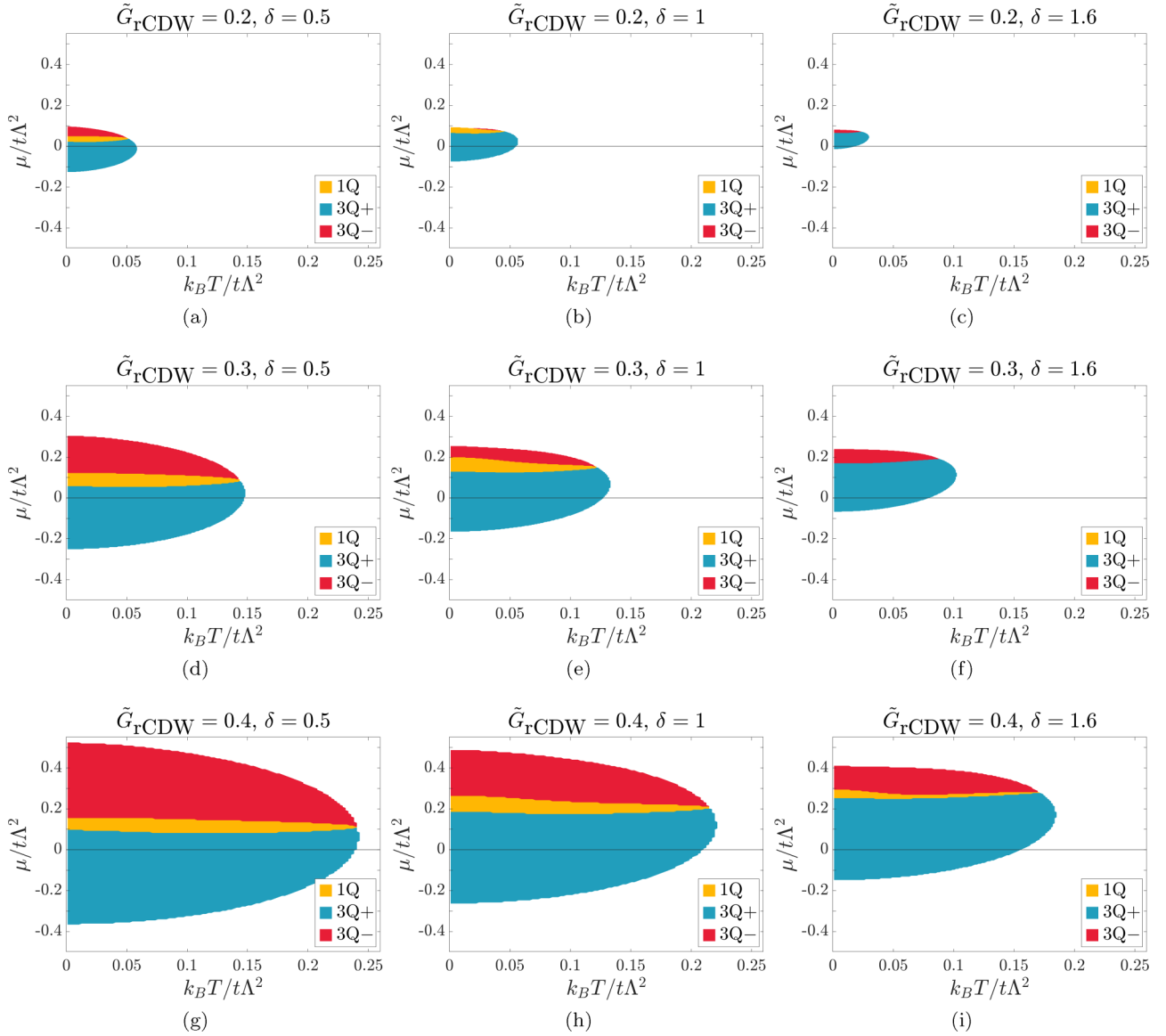


FIG. 6. rCDW phase diagrams calculated in the $k_B T$ - μ plane. $\tilde{G}_{\text{rCDW}} = G_{\text{rCDW}}/t\Lambda^2$ is defined as the dimensionless rCDW strength. δ parametrizes nesting as defined in Eq. (13). The phase diagrams correspond to the case $t, \delta > 0$ ($a, b > 0$ and $a/b > 1$). The phase diagrams for $t, \delta < 0$ ($a, b > 0$ and $a/b < 1$) are related to these phase diagrams under the exchange $3Q+ \leftrightarrow 3Q-$ and reflection in the $\mu = 0$ axis.

$2K_4$, the 3Q iCDW is favored. From the asymptotic solution shown in Fig. 5 at $\mu/t\Lambda^2 = 0.01$, we see that when $k_B T_c/t\Lambda^2 \lesssim 0.01$, and the 1Q iCDW is stable. When $k_B T/t\Lambda^2 \gtrsim 0.01$, $K_3 - 2K_4 < 0$. Thus, 3Q iCDW develops if T_c sits in this range of temperature, but it may become unstable to 1Q iCDW as temperature lowers. On the other hand, when $\mu \ll k_B T$, we find $K_3 - 2K_4 < 0$ in the low-temperature regime when $k_B T/t\Lambda^2 < 0.025$ (see Appendix D). Thus, 3Q iCDW should be stable at $\mu \sim 0$. This transition is a continuous phase transition in contrast to the rCDW case because of the absence of a third-order term. The real-space pattern for 1Q and 3Q iCDW orders are presented in Sec. VA2.

Next, we substitute the iCDW order parameter in Eq. (14) with the iCDW saddle-point solution, $|\phi_\alpha| = \phi^*$, and obtain the free energy for rCDW OPs. For 1Q iCDW, no rCDW can be induced. For 3Q iCDW, as the cubic term K_2 contains term linear in N_α through coupling to two iCDW OPs at another

two momenta, considering up to quadratic term in N , we find $\{N_1, N_2, N_3\} = N_0\{1, \pm 1, \pm 1\}$ up to any permutations of the signs between N_α , where $N_0 \sim \frac{K_2 \phi^{*2}}{(T - T_{\text{rCDW}})}$. Here, $T - T_{\text{rCDW}} \sim (\frac{1}{2G_{\text{rCDW}}} + K_1) > 0$. So the sign of N_0 is determined by the sign of K_2 . Since $K_2 < 0$ for $\mu/T \lesssim 2.14$, $N_0 < 0$, the induced rCDW order must be the $3Q-$ one. As temperature further lowers to $T < T_{\text{rCDW}}$, the quartic term in N_α should be included so that the free energy is stable. We checked that the rCDW order remains the $3Q-$ one for $K_2 < 0$ and vice versa.

D. rSDW-rCDW mean field theory

In phase III of the RG phase diagram, the rSDW is the leading density wave instability. Here, we consider how rCDW order can emerge as a subsidiary order through rSDW-rCDW coupling. Starting from the full interaction given by Eq. (3),

the rSDW interaction term is

$$H_{\text{rSDW}} = -\frac{\mathcal{N}G_{\text{rSDW}}}{2} \sum_{\alpha} \hat{\rho}_{\text{rS},\alpha} \cdot \hat{\rho}_{\text{rS},\alpha}, \quad (15)$$

where $\hat{\rho}_{\text{rS},\alpha} = \frac{|\epsilon_{\alpha\beta\gamma}|}{2\mathcal{N}} \sum_{|q|<\Lambda} c_{\beta q}^{\dagger} \frac{\sigma}{2} c_{\gamma q}$ is the spin density operator. Assuming the interaction in the rCDW channel is also attractive but much weaker than that of the rSDW channel, we can find the free energy to fourth order in the rSDW and rCDW order parameters. This gives us the rSDW free energy [which may be added to the rCDW free energy in Eq. (12)] [47]:

$$\begin{aligned} f_{\text{rSDW}} = & \left(\frac{1}{2G_{\text{rSDW}}} + \frac{K_1}{4} \right) \sum_{\alpha} |S_{\alpha}|^2 \\ & + \frac{K_2}{4} (N_1 S_2 \cdot S_3 + N_2 S_3 \cdot S_1 + N_3 S_1 \cdot S_2) \\ & + \frac{K_3}{16} \sum_{\alpha<\beta} |S_{\alpha}|^2 |S_{\beta}|^2 + \frac{K_4}{16} \sum_{\alpha} |S_{\alpha}|^4 \\ & + K_5 \sum_{\alpha<\beta} |S_{\alpha} \cdot S_{\beta}|^2 + K_6 (S_1 \cdot S_2 \times S_3)^2 + \dots \end{aligned} \quad (16)$$

Here, K_5, K_6 are new symmetry-allowed coefficients. The important aspect of this Landau theory is the third-order term which couples the rSDW and rCDW order parameters. This term is allowed by symmetry since it is invariant under time-reversal and lattice translation symmetry.

Close to the transition temperature T_c of the rSDW order, the terms involving rCDW order parameters can be treated as perturbations, so first we need the solution to Eq. (16). The rSDW Landau theory has already been thoroughly discussed in Ref. [47]. For chemical potential sufficiently close to the saddle point, the solution to the SDW Landau theory is a uniaxial 3Q rSDW phase where all three rSDW order parameters have the same magnitude and are oriented along the same axis, i.e., $S_{\alpha}^* = s n_{\alpha}$, where $n_{\alpha} = \pm 1$. If we substitute this solution into Eq. (16) and add the terms from Eq. (12), we get a free energy that is a function of just the rCDW OPs:

$$\begin{aligned} f_{\text{rCDW}} + f_{\text{rSDW}}|_{S_{\alpha}=S_{\alpha}^*} \\ = & \left(\frac{1}{2G_{\text{rCDW}}} + K_1 \right) \sum_{\alpha} N_{\alpha}^2 \\ & + \frac{K_2}{4} |s|^2 (n_2 n_3 N_1 + \text{cyc. perms.}) + K_2 N_1 N_2 N_3 \\ & + K_4 \left(\sum_{\alpha} N_{\alpha}^2 \right)^2 + (K_3 - 2K_4) \sum_{\alpha<\beta} N_{\alpha}^2 N_{\beta}^2. \end{aligned} \quad (17)$$

For $K_3 - 2K_4 < 0$, all terms prefer the 3Q+ rCDW state, so the system can develop a rCDW state.

V. EXTENSIONS AND EXPERIMENTAL IMPLICATIONS

In this section, we discuss various aspects of the different CDW phases, and how they may be differentiated experimentally.

A. Real-space rCDW and iCDW patterns

It is interesting to consider the real-space patterns of charges and currents associated with the rCDW and iCDW order parameters. Our continuum model does not carry any details of the lattice, so we rely on symmetry information provided by DFT calculations [58]. Importantly, as the saddle-point band at the three M points are even under inversion, it can be shown that among the d orbitals of vanadium atoms, only the α th vanadium atom in the unit cell contributes to the Bloch state at M_{α} (see Appendix A). Furthermore, the DFT calculation shows that the saddle points consist mostly of d orbitals of vanadium atoms. Motivated by these observations, we consider nearest-neighbor (NN) hopping on the kagome lattice as the minimal tight-binding model that should capture the essential physics from fermions near the saddle points. For convenience, the lattice coordinate for the three sublattices is expressed as $\mathbf{r}_{\alpha} = \mathbf{R} + \delta_{\alpha}$, where \mathbf{R} is the coordinate for a unit cell, whose origin is taken at the center of the triangular plaquette with the green sublattice facing to the left in Fig. 1(a). $\delta_1 = (-\frac{1}{2\sqrt{3}}, 0)$, $\delta_2 = (\frac{1}{4\sqrt{3}}, \frac{1}{4})$, and $\delta_3 = (\frac{1}{4\sqrt{3}}, -\frac{1}{4})$. The tight-binding Hamiltonian reads as

$$\hat{H}_0 = t_1 \sum_{\langle \mathbf{r}_{\alpha}, \mathbf{r}_{\alpha} + \mathbf{e}_{\beta} \rangle} d_{\mathbf{r}_{\alpha}}^{\dagger} d_{\mathbf{r}_{\alpha} + \mathbf{e}_{\beta}} + d_{\mathbf{r}_{\alpha} + \mathbf{e}_{\beta}}^{\dagger} d_{\mathbf{r}_{\alpha}}, \quad (18)$$

where $\langle \mathbf{r}_{\alpha}, \mathbf{r}_{\alpha} + \mathbf{e}_{\beta} \rangle$ is the NN bond and \mathbf{e} is defined such that $\mathbf{r}_{\gamma} = \mathbf{r}_{\alpha} + \mathbf{e}_{\beta}$ where $\{\beta, \alpha, \gamma\}$ is a permutation of $\{1, 2, 3\}$. This gives $\mathbf{e}_1 = \frac{1}{2}\{-1, 0\}$, $\mathbf{e}_2 = \frac{1}{2}\{-\frac{\sqrt{3}}{2}, \frac{1}{2}\}$, and $\mathbf{e}_3 = \frac{1}{2}\{\frac{\sqrt{3}}{2}, \frac{1}{2}\}$.

Due to the one-to-one correspondence between patch label M_{α} and sublattice label V_{α} of vanadium atoms, the real-space fermions on vanadium atoms can be expressed as

$$d_{\mathbf{r}_{\alpha}} = \frac{1}{\sqrt{\mathcal{N}}} \sum_k e^{i\mathbf{k} \cdot \mathbf{R}} d_{\alpha, \mathbf{k}} \approx \frac{1}{\sqrt{\mathcal{N}}} \sum_{|q|<\Lambda} e^{iM_{\alpha} \cdot \mathbf{R}} c_{\alpha q}, \quad (19)$$

where $c_{\alpha q}$ denotes the saddle-point fermion near M_{α} as defined in the continuous model [Eq. (1)]. As both rCDW and iCDW order parameters are condensates of interpatch fermion density operators, the associated real-space order must be a *bond order* on the kagome lattice. For simplicity, we will consider only nearest-neighbor (NN) bond order as an example.

1. rCDW pattern

The rCDW order parameter is time-reversal even, and contributes to bond density modulation as

$$\begin{aligned} \langle \delta \hat{\rho}_{\mathbf{r}_{\alpha}, \mathbf{r}_{\alpha} + \mathbf{e}_{\beta}} \rangle & = \langle \delta \hat{\rho}_{\mathbf{r}_{\alpha}, \mathbf{r}'_{\gamma}} \rangle = \text{Re}[\langle d_{\mathbf{r}_{\alpha}}^{\dagger} d_{\mathbf{r}_{\alpha} + \mathbf{e}_{\beta}} \rangle] \\ & = \frac{N_{\alpha\gamma}}{G_{\text{rCDW}}} \cos(M_{\alpha} \cdot \mathbf{R} - M_{\gamma} \cdot \mathbf{R}'), \end{aligned} \quad (20)$$

where $\mathbf{r}'_{\gamma} = \mathbf{r}_{\alpha} + \mathbf{e}_{\beta} = \mathbf{R}' + \delta_{\gamma}$ with $\gamma \neq \alpha \neq \beta$. In Fig. 7, the rCDW charge bond density modulation is shown for the 3Q± and 1Q rCDW states.

2. iCDW pattern

The iCDW order parameter breaks time-reversal symmetry and corresponds to bond current in real space. Note that the current operator is well defined only when the charge is

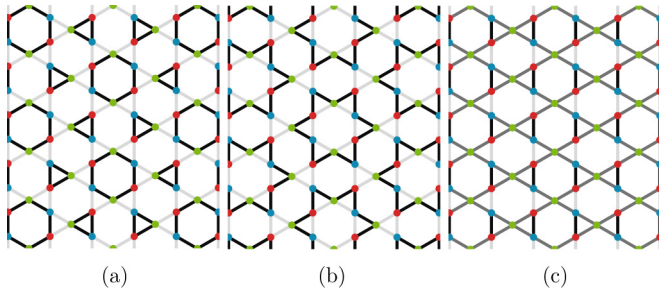


FIG. 7. Real-space rCDW bond order pattern of the 3Q \pm and 1Q configurations. Configurations in the 3Q \pm classes are related by translation. Configurations in the 1Q class are related by translation and a threefold rotation. (a) Bond ordering corresponding to the 3Q+ rCDW class. The bond ordering forms hexagonal and triangular plaquettes. (b) Bond ordering corresponding to the 3Q- rCDW class. The bond ordering forms a star of David pattern. (c) Bond ordering pattern corresponding to the 1Q rCDW class. The pattern has alternating bond strength along one direction and uniform strength in the other two bond directions.

conserved, which is indeed the case in both the high-temperature disordered phase and iCDW phase. As a result, in the equilibrium phase, the current operator must satisfy

$$\sum_{\mathbf{r}_\alpha \rightarrow \mathbf{r}'_\alpha} \hat{j}_{\mathbf{r}_\alpha \mathbf{r}'_\alpha} = 0. \quad (21)$$

By comparing the continuity equation and the equation of motion for charge density, we find the current operator on the NN bonds as (see Appendix E)

$$\begin{aligned} \hat{j}_{\mathbf{r}_\alpha \mathbf{r}'_\alpha} &= \hat{j}_{\mathbf{r}_\alpha \mathbf{r}_\alpha + \mathbf{e}_\beta} \delta_{\mathbf{r}'_\alpha, \mathbf{r}_\alpha + \mathbf{e}_\beta} \delta_{\alpha \neq \beta} \\ &= \frac{ie}{\hbar} t_1 (d_{\mathbf{r}_\alpha}^\dagger d_{\mathbf{r}_\alpha + \mathbf{e}_\beta} - d_{\mathbf{r}_\alpha + \mathbf{e}_\beta}^\dagger d_{\mathbf{r}_\alpha}), \end{aligned} \quad (22)$$

where t_1 is the NN hopping defined in Eq. (18). From Eq. (19), the bond current expectation value can be expressed in terms of iCDW order parameter as

$$\begin{aligned} \langle \hat{j}_{\mathbf{r}_\alpha \mathbf{r}_\alpha + \mathbf{e}_\beta} \rangle &= \langle \hat{j}_{\mathbf{r}_\alpha \mathbf{r}'_\alpha} \rangle \\ &= ie t_1 e^{-i(\mathbf{M}_\alpha \cdot \mathbf{R} - \mathbf{M}_\gamma \cdot \mathbf{R}')} \\ &\quad \times \left(\frac{1}{\mathcal{N}} \sum_q (\langle c_{\alpha, q}^\dagger c_{\gamma, q} \rangle - \langle c_{\gamma, q}^\dagger c_{\alpha, q} \rangle) \right) \\ &= \frac{-2e t_1}{G_{\text{iCDW}}} e^{-i(\mathbf{M}_\alpha \cdot \mathbf{R} - \mathbf{M}_\gamma \cdot \mathbf{R}')} \phi_{\alpha\gamma}, \end{aligned} \quad (23)$$

where again we used $\mathbf{r}'_\gamma = \mathbf{r}_\alpha + \mathbf{e}_\beta = \mathbf{R}' + \delta_\gamma$ with $\gamma \neq \alpha \neq \beta$. From Eq. (23), the real-space bond current pattern from ϕ_{23} is shown in Fig. 8(a). The linear combinations of them can form loop current; as an example, we show the bond current pattern for $\{\phi_{23}, \phi_{31}, \phi_{12}\} = \phi_0\{1, 1, 1\}$ in Fig. 8(b).

The primary order parameter for the iCDW is a loop current. However, as was discussed in Sec. IV C, from the form of the K_2 coupling terms in Eq. (14), a 3Q iCDW will also induce charge order. In particular we see that a 3Q iCDW induces either a 3Q+ or 3Q- state depending upon the sign of K_2 . Notably, the charge order is quadratic in the iCDW

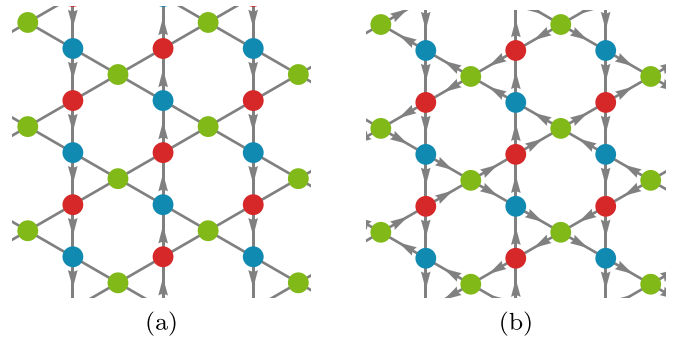


FIG. 8. Real-space iCDW (current) bond order pattern of the (a) 1Q and (b) 3Q states. All 3Q configurations are related by translations or time reversal (changing the sign of the currents). Configurations in the 1Q class are related by translation (i.e., reversing the current direction) and a threefold rotation. Note that the 1Q state is macroscopically time-reversal symmetric because it is invariant under the combination of time-reversal and translation. (a) Bond current in the 1Q class, with $\{\phi_{23}, \phi_{31}, \phi_{12}\} = \phi_0\{1, 0, 0\}$. (b) Bond current from $\{\phi_{23}, \phi_{31}, \phi_{12}\} = \phi_0\{1, 1, 1\}$. The sign of ϕ_0 is taken as negative here.

order parameter, $N_\alpha \sim \phi^2$, which could be detectable near the transition temperature.

B. Three-dimensional coupling

Here we extend the Landau theory to consider the implications of coupling of CDW order parameters between nearby layers, adding a layer index $z = 0, 1, 2, \dots$ numbered beginning from the top layer. We assume this coupling is weak, so can be approximated by the leading terms linear in the order parameters in each layer, and decays rapidly with the distance between layers. Hence,

$$f_\perp = \sum_{z=0}^{\infty} \sum_{\delta=1}^{\infty} (K_{\perp, \delta} N_{\alpha, z} N_{\alpha, z+\delta} + L_{\perp, \delta} \phi_{\alpha, z} \phi_{\alpha, z+\delta}). \quad (24)$$

We assume that all the interlayer interactions are weak compared to the intralayer terms in the free energy, so that the form of the order within each layer is established by the latter, and the intralayer terms serve to select particular relative orientations of the different symmetry-breaking states in nearby layers. Here we expect $|K_{\perp, 1}| \gg |K_{\perp, \delta > 1}|$ and $|L_{\perp, 1}| \gg |L_{\perp, \delta > 1}|$ so that terms with $\delta > 1$ can be neglected unless they are required to break degeneracies.

1. Three-dimensional ground states

Now we discuss the resulting three-dimensional ordered structures. First consider the imaginary CDW, within the 3Q phase. Within a given layer, ϕ_α may take one of the values $\phi_\alpha = |\phi_0|(\pm 1, \pm 1, \pm 1)$, where all eight signs are possible, and $|\phi_0|$ is fixed by single-layer energetics. If $L_{\perp, 1} < 0$, the minimum energy iCDW order parameter is identical in all layers, $\phi_{\alpha, z} = \phi_\alpha$. If instead, $L_{\perp, 1} > 0$, the minimum energy configuration is “antiferromagnetic,” $\phi_{\alpha, z} = (-1)^z \phi_\alpha$. The two cases above correspond to an ordering wave vector with the z component $k_z = 0, \frac{1}{2}$, in lattice units. Note that $k_z = \frac{1}{2}$

is the wave vector for the current order, but the induced real CDW order would have $q_z = 0$ in both cases.

Now consider the real CDW, in either the 3Q+ or 3Q− states. Within a single layer, N_α may take just four values, with $N_\alpha = N_0 n_\alpha$, with $n_\alpha^2 = 1$ and $n_1 n_2 n_3 = 1$. For $K_{\perp,1} < 0$, we again obtain a “ferromagnetic” state, with $N_{\alpha,z} = N_\alpha$. For $K_{\perp,1} > 0$, however, the situation is distinct from the iCDW case, because an overall sign change in N_α is not permitted. Instead, for a given state $n_{\alpha,z}$, the interlayer coupling equally favors $n_{\alpha,z+1}$ in any of the three states not equal to $n_{\alpha,z}$. For N layers, the total degeneracy of ground states, consider just the $K_{\perp,1}$ interaction, is $4 \times 3^{N-1}$, a macroscopic degeneracy including states with arbitrary wave vectors k_z . We must therefore consider further-neighbor interactions. The problem can be mapped to a four-state Potts model, by defining the four allowed configurations of N_α in a single layer as $\sigma = 1 \dots 4$. The interaction energy becomes

$$f_{\perp} = \sum_{z=0}^{\infty} \sum_{\delta=1}^{\infty} K_{\perp,\delta} N_0^2 (4\delta_{\sigma_z, \sigma_{z+\delta}} - 1), \quad (25)$$

which illustrates the S_4 permutation symmetry of a Potts model. This is a four-state Potts chain with competing further-neighbor interactions, which has a rich statistical mechanics for general couplings, similar to that of the axial next-nearest-neighbor Ising (ANNNI) model, a paradigm for devil’s staircases, commensurate and incommensurate phases, and transitions between them. Here because each Potts spin represents an entire 2D layer, the energies involved are proportional to the area of a layer, and hence much larger than $k_B T$. Therefore, we are interested only in the ground states of the Potts chain. In this limit, the ground states are generally commensurate, but can have very large unit cells (in the z direction), and the devil’s staircase can arise. We limit our discussion to only the simplest cases, and assume $|K_{\perp,\delta}| \gg |K_{\perp,\delta+1}|$ as expected on grounds of locality.

The simplest situation is $K_{\perp,2} < 0$, in which case second-neighbor layers prefer to be parallel. We have then alternating states in successive layers, $\sigma_z = \sigma_1$ for z even and $\sigma_z = \sigma_2$ for z odd, with $\sigma_1 \neq \sigma_2$. In terms of the rCDW vector, $n_{\alpha,z} = n_\alpha^{(1)}$ for z even and $n_{\alpha,z} = n_\alpha^{(2)}$ for z odd, such that $\mathbf{n}^{(1)} \cdot \mathbf{n}^{(2)} = -1$. This corresponds to the wave vector $k_z = \frac{1}{2}$ in lattice units. Note that the three-dimensional degeneracy of this state is $4 \times 3 = 12$.

If $K_{\perp,2} > 0$, then we require both nearest-neighbor and second-neighbor Potts spins to differ in the ground state. After choosing the first layer, there are three choices for the second layer, and then two choices for the third layer, which must be distinct from the first two layers. This implies the smallest possible periodicity of the ground state is 3. It may, however, be larger. Indeed for the fourth layer, there are still two choices remaining, and the ground state is not determined. To fix this degeneracy, we may yet consider the third-neighbor coupling. If $K_{\perp,3} < 0$, then we favor a return to the original state. The entire configuration becomes determined, with a periodicity of 3, and a representative sequence in Potts variables like $\sigma_z = 1, 2, 3, 1, 2, 3, 1, 2, 3, \dots$. These configurations correspond to a “chiral” ordering of the layers, consistent with a threefold screw axis. Alternatively, if $K_{\perp,3} > 0$, then we obtain a four-layer periodicity $\sigma_z = 1, 2, 3, 4, 1, 2, 3, 4, \dots$

These two situations have smaller ordering wave vectors in the z direction, $k_z = \frac{1}{3}, \frac{1}{4}$, respectively. Note that the relatively simple results quoted here are the result of assuming a strict hierarchy of interactions, with couplings decaying rapidly in strength with the separation of layers. Otherwise, much more complex states may arise in the Potts chain.

We conclude that a distinct difference between the iCDW and rCDW is the presence of periodicities larger than 2 in the c direction. Appearance of such a periodicity (i.e., $k_z = \frac{1}{3}, \frac{1}{4}$) would provide clear experimental evidence in favor of the real over the imaginary CDW.

2. Rotational symmetry breaking

In the previous discussion, we determined the relative ordering between layers assuming the order parameter within each layer is rigid. Now we consider a higher-order effect: the back influence of the interlayer interaction on the order parameter within a single layer. In particular, in the case of rCDW order, this leads to a breaking of C_3 rotational symmetry within a given layer. This can be understood as follows. All four of the 2D ordered states in the 3Q+ or 3Q− states preserve C_3 symmetry around the centers of one of the four hexagons within the quadrupled unit cell, but not around the other three. In the states with $k_z > 0$, the centers of neighboring layers are not aligned. Consequently, there is no rotation axis which preserves all layers. In the chiral $k_z = \frac{1}{3}$ states, there is instead a screw axis, which preserves macroscopic C_3 symmetry of the crystal in the bulk. This symmetry is, however, broken at the surface. In the states with $k_z = \frac{1}{2}, \frac{1}{4}$, there is not even macroscopic C_3 symmetry.

In all cases, if one observes the order within a single layer, its neighbors will influence its order and lower the symmetry. The situation is simplest for the top layer. Assume the system develops long-range order, and therefore we may treat the interlayer interaction in a mean field sense. We therefore replace the coupling to the second layer from the top (the strongest such coupling) by a term of the form

$$f_{\perp,0} = K_{\perp,1} \langle N_{\alpha,1} \rangle N_{\alpha,0}. \quad (26)$$

This term appears as a “field” on the order parameter in the top layer ($z = 0$). In, for example, the $k_z = \frac{1}{2}$ phase, we may take $\langle N_{\alpha,1} \rangle = N_0(1, 1, 1)$. Then, these configurations in the first layer are “pushed” away from the $(1, 1, 1)$ direction. For example, if the top layer chooses the $(1, \bar{1}, \bar{1})$ state, the interlayer coupling will shift it to the form $N_{\alpha,0} = N_0(1 - \delta, -1 - \delta, -1 - \delta)$, with $0 < \delta \ll 1$. Note that $|N_1| < |N_2| = |N_3|$. The consequence is that the two-dimensional Bragg peaks associated to density oscillations in the top layer develop two unequal magnitudes. This is a sign of the rotational symmetry breaking. Indeed, one can define a two-dimensional vector $\mathbf{v}_{z,z'} = -\mathbf{v}_{z',z}$,

$$\mathbf{v}_{z,z'} = \sum_{\alpha} \langle n_{\alpha,z} n_{\alpha,z'} \rangle \mathbf{a}_{\alpha}, \quad (27)$$

where \mathbf{a}_{α} are the 2D triangular Bravais lattice vectors with $\mathbf{a}_3 = -\mathbf{a}_1 - \mathbf{a}_2$. The vector $\mathbf{v}_{z,z'}$ is oriented along one of the three principal directions and selects this axis.

This rotational symmetry-breaking effect exists within each layer in all the 3Q± rCDW phases except the uniform

$k_z = 0$ one. Rotational symmetry is also broken in the bulk (i.e., in an infinite system in the z direction) *except* when it is restored macroscopically by an arrangement of layers that constitutes a screw axis. The latter occurs only for the $k_z = \frac{1}{3}$ case detailed above. Rotational symmetry breaking is, however, absent both in individual layers and in bulk, in the 3Q iCDW states, providing another means to differentiate the iCDW from the rCDW experimentally.

C. Critical behavior

We briefly discuss the expected critical behavior at the ordering temperature for some important cases based on the symmetries and order parameters. This question is motivated by the presence of a cubic term in the rCDW Landau theory, which might suggest a first-order transition to the CDW state, which to our knowledge is not observed experimentally. While a full understanding is somewhat involved, we argue below that both thermal fluctuations in two dimensions and three-dimensional coupling stabilize a continuous transition within most scenarios.

1. Two dimensions

If we neglect interlayer coupling, the problem becomes two dimensional, and we must be wary of applying a mean field Landau theory analysis to critical properties since it is well known that two-dimensional systems have strong thermal fluctuations.

For the case of the 3Q+ or 3Q− rCDW, as discussed in Sec. VB1, the ordering can be described by a four-state Potts model. At mean field level, the q -state Potts models have first-order transitions for $q \geq 3$, consistent with the Landau analysis. It is well known, however, that in two dimensions the $q = 3, 4$ Potts models in fact have continuous transitions described by conformal field theory. In particular, the $q = 4$ Potts model is equivalent to the Ashkin-Teller model, and has known critical exponents with logarithmic corrections due to marginal operators (see, e.g., Ref. [63]).

In the case of the 3Q iCDW, the order parameter has a degeneracy of 8 and transforms under full cubic O_h symmetry, and we have seen that it can be expressed as an $O(3)$ vector with cubic anisotropy. In two dimensions, this problem has been analyzed by Schick [64], who concludes that the transition to the 3Q phase (called “corner cubic anisotropy” in this reference) may be either continuous (and in the Ising universality class, surprisingly) or first order.

2. Three dimensions

The two-dimensional critical behavior is valid at best in a regime close but not too close to the critical point, where a crossover to three-dimensional behavior must occur. The nature of the true three-dimensional critical regime is, however, dependent on the type of interlayer couplings, and thereby the three-dimensional order parameter. As discussed in Sec. VB1, this is rather complicated for the rCDW problem, and we will not offer a complete analysis. The simplest case is the $k_z = 0$ one, which occurs when the interlayer coupling favors ferromagnetically aligned rCDWs. Then, the symmetry remains unchanged from the four-state Potts model. However,

in three dimensions, this model has a first-order transition. Thus, in this case a first-order transition is predicted. If instead one of the $k_z > 0$ orderings occur, the situation is less clear, but it is manifestly *not* a Potts model transition. It is natural to think that the Landau analysis is more correct in three dimensions. Based on this reasoning, for the cases $k_z = \frac{1}{2}$ and $\frac{1}{4}$, a cubic term in the order parameter is no longer allowed by momentum conservation. Thus, a continuous transition may be expected. The case $k_z = \frac{1}{3}$ seems to allow a cubic term but we will not pursue it further here.

With three-dimensional coupling, the iCDW order develops either at $k_z = 0$ or $\frac{1}{2}$. In both cases, the three-dimensional order parameter remains an $O(3)$ vector with cubic anisotropy, and the ground-state degeneracy is unchanged from 8 (this can be seen because even in the $k_z = \frac{1}{2}$ can a translation by one layer is equivalent to time reversal). Hence, the transition should be in the $O(3)$ cubic universality class, which is known to be continuous, and is discussed, e.g., in Ref. [65].

D. Magnetic moment induced by iCDW order

The iCDW order can induce both staggered magnetic moment due to the loop current and uniform magnetic moment. Here, we estimate the magnitude from each contribution.

First, we note that the bond current obtained in Eq. (23) is linear in ϕ , consequently, only the Fourier component at \mathbf{M} contributes to the bond current, and there is no uniform magnetic moment induced by the bond current. To estimate the staggered magnetic moment, we consider the 3Q iCDW order as an example. As shown in Fig. 8(b), the bond current forms loop current around both the honeycomb and triangular plaquettes. Treating each plaquette as a current loop, its magnetic moment and the magnetic field it induces can be obtained following the standard magnetostatics [66]. Due to the 2×2 sublattice structure, there are two types of honeycomb plaquettes, with $\mathbf{m}_{h,1} = I_e \hat{A}_h$ for one-quarter of the honeycomb plaquettes, and $\mathbf{m}_{h,2} = -I_e \hat{A}_h/3$ for the rest. Similarly, one-quarter of the triangular plaquettes have $\mathbf{m}_{t,1} = -I_e \hat{A}_t$, and the rest have $\mathbf{m}_{t,2} = I_e \hat{A}_t/3$. Here, $I_e = -\frac{e}{\hbar} \frac{2t_1}{G_{\text{iCDW}}} \phi_0$ denotes the magnitude of the electric loop current. $\hat{A}_{h,t}$ is along \hat{z} , such that for $I_e > 0$, the current flows counterclockwise. And its magnitude is determined by the area of the honeycomb (h) and triangular (t) plaquette. In unit of Bohr magneton $\mu_B = \frac{e\hbar}{2m_e}$, we have $\mathbf{m} \sim I_e \hat{A} = -\frac{2t_1}{G_{\text{iCDW}}} \frac{\phi_0}{Ry} \frac{\hat{A}}{a_b^2} \mu_B$, where $Ry = \frac{m_e e^4}{32\pi^2 \epsilon_0^2 \hbar^2} \approx 13.6$ eV is the Rydberg energy, $r_b = \frac{4\pi\epsilon_0\hbar}{m_e e^2} \approx 5.29 \times 10^{-11} m$ is the Bohr radius. In I_e , the factor $\frac{2t_1}{G_{\text{iCDW}}}$ is dimensionless and scales with the polarization bubble $\sim \ln^2(t\Lambda^2/T_c) \sim O(1)$, the order parameter (in unit of energy) at low temperature can be approximated as $\phi_0 \sim k_B T_c$, where T_c is the transition temperature for iCDW order. This gives $\mathbf{m}_{h,1} \approx -0.047 \text{sgn}(\phi_0) \mu_B \hat{z}$, $\mathbf{m}_{t,1} \approx 0.008 \text{sgn}(\phi_0) \mu_B \hat{z}$, where we take $2t_1/G_{\text{iCDW}} = 1$. We also note that similar analysis has been done in the literature for cuprates [67] and iron-pnictides [68].

Next, we discuss the uniform magnetization induced by the iCDW order. On the symmetry ground, uniform magnetization requires iCDW order at all three momenta \mathbf{M} nonzero. Otherwise, the system is invariant under the

antiunitary symmetry composed of time reversal and translation, which forbids any uniform magnetization. In general, the magnetic field couples to the electrons through both the minimal coupling and the Zeeman coupling. Here, we consider the orbital magnetization contribution for the $3Q\pm$ iCDW order. Following [69], the orbital magnetization in terms of the Bloch wave function reads as

$$\mathcal{M}_{\text{orb}}^z = \frac{e}{2\hbar} \sum_{n,\mathbf{q}} \text{Im}[\langle \partial_{\mathbf{q}} \mathbf{u}_{n,\mathbf{q}} \times [\epsilon_{n,\mathbf{q}} - \hat{H}_{\text{MF}}(\mathbf{q})] | \partial_{\mathbf{q}} \mathbf{u}_{n,\mathbf{q}} \rangle] f_{n,\mathbf{q}}, \quad (28)$$

where $\hat{H}_{\text{MF}}(\mathbf{q})$ is the mean field Hamiltonian one can infer from Eq. (8), $f_{n,\mathbf{q}} = f(\epsilon_{n,\mathbf{q}} - \mu)$ is the equilibrium Fermi distribution function.

For simplicity, we consider the perfect nesting case when the Fermi energy in the disordered phase is at the van Hove point; this gives $\frac{1}{3}$ filling in the patch model. When the $3Q$ iCDW order is present, the triple degenerate bands at the \mathbf{M} points are fully gapped, and only the lowest band is filled. Noting that the unit of the summand in Eq. (28) is $\frac{\hbar^2}{2m_e}$ (coming from the kinetic energy), for a filled band, the summand must be expressed as a function of the only dimensionless parameter in the expression, which reads as $\tilde{\epsilon} = \hbar^2 q^2 / (2m_e)$, i.e., the summand (after averaging over the angular direction in \mathbf{q}) must be expressed as $\sim \frac{\hbar^2}{2m_e} \mathcal{F}(\tilde{\epsilon})$. This means physically that for electrons within an energy of order the gap ϕ , the typical orbital moment is an order-one fraction of a Bohr magneton.

The orbital magnetization can be expressed as

$$\begin{aligned} \mathcal{M}_{\text{orb}}^z &= \frac{e\hbar}{2m_e} \mathcal{N} \frac{\phi_0}{\hbar^2 / (2m_e a_0^2)} \frac{\sqrt{3}}{2\pi} \left[\int_0^\Lambda d\tilde{\epsilon} \mathcal{F}(\tilde{\epsilon}) \right] \\ &= \mathcal{N} \mu_B \frac{\phi_0}{R_y} \left(\frac{a_0}{a_b} \right)^2 \frac{\sqrt{3}}{2\pi} \mathcal{I}_F, \end{aligned} \quad (29)$$

where \mathcal{N} is the number of unit cells, $\mathcal{I}_F = \int_0^\Lambda d\tilde{\epsilon} \mathcal{F}(\tilde{\epsilon})$ is the value of the integral, which is bounded and can be computed numerically as $\mathcal{I}_F \approx -0.87$. Again approximating $\phi_0 \sim k_B T_c$, the orbital magnetization per unit cell is $\mathcal{M}_{\text{orb}}^z / \mathcal{N} \sim -0.017 \text{sgn}(\phi_0) \mu_B$.

This orbital magnetization is small but the smallness is primarily due to the small number of electrons within the region near the energy gap. As remarked above, for a typical electron within this region, the orbital moment is a substantial fraction of μ_B . This suggests that the iCDW state may be favored by the application of a magnetic field.

We consider, therefore, how an rCDW state may be converted into an iCDW state by such a field, assuming the energy of the iCDW state is not too much higher than that of the rCDW in zero field. For simplicity we consider low temperature, where the above estimate is valid (near T_c , the orbital magnetization will be proportional to ϕ^3 , and greatly suppressed). In general, a magnetic field breaks time reversal, so will always induce some iCDW component if the rCDW is present. We thus take $\Delta_\alpha = N_\alpha + i\phi_\alpha = |\Delta| e^{i\theta}$ (assuming a $3Q+$ state), and express the energy in terms of $|\Delta|$ and θ . A simplified form for the energy density is

$$\mathcal{E} = -m|\Delta|^2 (1 + \lambda \cos \theta) - \mu h m |\Delta| \sin \theta, \quad (30)$$

where m is the mass scale for the saddle points, h is the magnetic field (in the z direction), μ is a typical orbital moment for the iCDW electrons, and is a fraction of μ_B . The first term is the condensation energy of the CDW, and the second term is the dipole energy associated with the orbital magnetization. The parameter $\lambda > 0$ describes the energetic preference for rCDW over iCDW order in zero field (as well as the preference for $3Q+$ over $3Q-$ order). When the competition between the two is close, $\lambda \ll 1$. Minimizing over θ , we obtain

$$\tan \theta = \frac{\mu h}{\lambda |\Delta|}. \quad (31)$$

We see that the rCDW smoothly evolves into an iCDW with applied field, and this occurs on a scale which can be a small fraction of the gap, if $\lambda \ll 1$. We note that the energy density in Eq. (30) is simplified, and does not capture topological physics relevant to the perfect nesting situation when the system is doped exactly to the saddle-point filling. In this case, the system is a trivial insulator for $\theta = 0$, and a Chern insulator for $\theta = \pi/2$, and hence there must be a topological transition, associated gap closing, and nonanalyticity of the energy at some intermediate angle. However, we expect this distinction to be washed out away from perfect nesting and for generic filling.

VI. SUMMARY

In this paper, we have discussed various mechanisms to induce charge density wave order in kagome metals, motivated by experiments on the AV_3Sb_5 materials. We began with a g -ology description based on a continuum saddle-point model, which is quite general to two-dimensional materials with hexagonal symmetry, and was originally introduced in the context of doped graphene in Ref. [46]. We extended the renormalization group analysis of this problem to the general case, i.e., with both repulsive and attractive bare interactions, and showed that several distinct density wave and superconducting instabilities are possible, depending upon parameters. We also showed that the attractive bare interactions may come from coupling of electrons to optical phonons, which induces attraction in certain channels (g_i) and lowers the phonon energy. The latter effect may be relevant to the phonon softening observed in *ab initio* calculations [70]. Our focus then turned to charge density wave order at the vectors \mathbf{M}_α , which correspond both to the locations of the saddle points in the Brillouin zone and the spanning vectors between them. They are half-reciprocal lattice vectors and reside at the centers of the zone faces. We applied a mean field theory to the real charge density wave (rCDW) states of the continuum interacting model, and found isotropic $3Q\pm$ as well as nematic $1Q$ rCDW states occur and may be tuned by chemical potential. We also carried out a Landau theory analysis of the rCDW orders (and a detailed derivation of the Landau theory coefficients from the continuum model) which shows that when this is the leading instability, the above states are the only ones that occur with a high degree of generality. Next, we considered the alternate cases of a $3Q$ imaginary charge density wave (iCDW), actually a state of circulating currents, i.e., orbital moments, and a spin density wave (rSDW), which

are competing instabilities with the same wave vectors. We showed that both iCDW and rSDW can induce rCDW order, though in both cases the charge density order is then not the primary order parameter. Finally, we detailed a number of extensions and implications of the analysis to derive explicit charge and current patterns, three-dimensional ordered states, critical properties, and orbital magnetization of the 3Q iCDW state.

What are the specific implications of these results for the AV_3Sb_5 materials? Three distinct compounds, with $A = K, Cs, Rb$, have been studied to our knowledge. All are known to show rCDW order for which the projection of the ordering wave vector to the 2D kagome plane is of the 3Q M_α type. A key question is whether the rCDW is the primary order parameter, or whether it is secondary and induced, as discussed above, by either an iCDW or rSDW order. Notably, both the iCDW and rSDW orders break time-reversal symmetry, and hence should be detectable via their induced local magnetic moments through, e.g., muon spin resonance or neutron scattering. To our knowledge, there is no direct evidence of time-reversal breaking from any measurement in zero magnetic field (and there is some counterevidence from muon spin resonance on KV_3Sb_5 [26]). This does not definitively exclude states with very small moments, as indeed may be expected in the iCDW case (cf. Sec. VD). The discussion of three-dimensional order in Sec. VB1 provides some more clear diagnostics. There, we showed that the iCDW is expected to display identical induced rCDW order in all layers, i.e., the z component of the rCDW ordering wave vector should be zero. By contrast, a pure rCDW is consistent with $k_z = 0, \frac{1}{2}, \frac{1}{3}, \frac{1}{4}$. Moreover, rCDW states with $k_z \neq 0$ should show “nematic” C_3 rotational symmetry breaking at the surface, due to the three-dimensional coupling, which again is not expected in the iCDW states.

Several experimental papers are directly related to the above aspects of the CDW order. X-ray scattering found Bragg peaks associated with three-dimensional CDW order with $k_z = \frac{1}{2}$ in RbV_3Sb_5 and CsV_3Sb_5 in Ref. [22], $k_z = \frac{1}{4}$ in CsV_3Sb_5 in Ref. [27]. Reference [24] measured an in-plane shift of the order in the top two layers of CsV_3Sb_5 across a step edge using STM, indicating $k_z > 0$. These observations are consistent with primary rCDW order. Reference [36] measured a “nematic” (i.e., C_2 -symmetric) dependence of the c -axis resistivity in CsV_3Sb_5 on an in-plane magnetic field in the normal (but CDW) state up to about 60 K, $\frac{2}{3}$ of the critical temperature. Such behavior would be expected below the CDW T_c for any rCDW except the “screw” state with $k_z = \frac{1}{3}$. The STM study in Ref. [20] notes differences in the intensities of the three charge order wave-vector peaks in KV_3Sb_5 . This reference concludes that the three intensities are all unequal, and denote this as a “chiral” charge order. To our eyes, their Fourier transform STM data [Figs. 3(a)–3(c) of Ref. [20]] is better described by two strong and approximately equal intensities and one weaker one, which is consistent with our theory of interlayer coupling. A very recent paper reports the latter type of anisotropy in independent STM measurements of KV_3Sb_5 [71].

While the above evidence seems to favor primary rCDW order, iCDW or SDW states might be realized in some situations, e.g., as competing orders that appear at lower tem-

peratures or induced through applied fields. Indeed, the early observation of large anomalous Hall effect [72] in KV_3Sb_5 motivated several later works to promote the possibility of an iCDW (recently similar behavior was observed in CsV_3Sb_5 [38]). As discussed in Sec. VD, the 3Q iCDW does indeed macroscopically break time reversal and is accompanied by a uniform orbital moment and a large Berry curvature in the vicinity of the saddle points, which should induce an anomalous Hall effect. We discussed how, if iCDW order is only slightly higher in energy than rCDW, the iCDW can be induced by modest applied fields, which may provide a possible explanation of Ref. [72]. Further study of the anomalous Hall effect and its correlation with other measurements is, however, needed to test this possibility.

Note added. Recently, several theoretical works appeared discussing density wave order in these materials. Reference [73] evaluated the mean field ground-state energies for multiple density wave orders. Reference [74] considered a single orbital extended Hubbard model on the kagome lattice, and within mean field theory found dominant iCDW order. Reference [75] discusses a coupled mean field theory of spin and charge orders and Chern bands in a continuum saddle-point model similar to the one used here and postulates a complex CDW state in the AV_3Sb_5 materials with three unequal magnitudes of CDW at the three M_α wavevectors.

In this paper, we have focused on density wave order, which is clearly the dominant instability in the AV_3Sb_5 materials. However, the superconductivity occurring at lower temperature is of considerable interest as well. Since it occurs *within* the density wave ordered state, the understanding of the latter should be important for developing a theory of superconductivity in this family.

ACKNOWLEDGMENTS

We acknowledge useful discussions with S. Wilson, B. Ortiz, S. Teicher, and I. Zeljkovic. L.B. is supported by BES Award No. DE-SC0020305. M.Y. is supported in part by the Gordon and Betty Moore Foundation through Grant No. GBMF8690 to UCSB and by the National Science Foundation under Grant No. NSF PHY-1748958. T.P. was supported by the National Science Foundation through Enabling Quantum Leap: Convergent Accelerated Discovery Foundries for Quantum Materials Science, Engineering and Information (Q-AMASE-i) Award No. DMR-1906325.

APPENDIX A: IRREDUCIBLE REPRESENTATIONS AT M_α

As shown in Fig. 2, there are two saddle points at M_α . The little cogroup at M_α is D_{2h} , and the irreps of the two saddle points at M_1 are Γ_1^+ and Γ_3^+ . The convention used here is the one used in Ref. [59], and the orientation of the two symmetry axes are shown in Fig. 1(a).

Now, we explain the one-to-one correspondence between the Brillouin zone patches M_α and the vanadium sites V_α . Consider how Bloch states formed from s orbitals placed on the vanadium sites (V_1, V_2, V_3) transform at M_1 . A s -orbital Bloch wave on V_1 transforms as the irrep Γ_1^+ . On the other hand, s orbitals placed on V_2, V_3 form a reducible

representation that can be decomposed into the $\Gamma_2^- + \Gamma_4^-$ irreps. Notice that the irrep of the s orbital on V_1 is even under inversion, but the irreps of the s orbitals on the V_2, V_3 sites are odd under inversion. Since d orbitals are even under inversion, this means that Bloch states formed from d orbitals at V_1 must be even under inversion, but Bloch states formed from d orbitals on V_2, V_3 must be odd under inversion. The saddle points at \mathbf{M}_1 are even under inversion; therefore, only the d orbitals on the V_1 site contribute to the saddle point at \mathbf{M}_1 . Using a threefold rotation, it is easy to see that at $\mathbf{M}_2, \mathbf{M}_3$, the contribution to the bands must come from d orbitals on the V_2, V_3 sites, respectively. Hence, there is a one-to-one correspondence between the Brillouin zone patches \mathbf{M}_α and the vanadium sites V_α . Away from \mathbf{M}_1 , d orbitals on V_2, V_3 can start mixing with the saddle-point bands, but we assume these contributions are small sufficiently close to \mathbf{M}_1 .

APPENDIX B: MICROSCOPIC MECHANISM OF ATTRACTIVE FERMION INTERACTION

Generally, pure electronic interactions, i.e., the screened Coulomb repulsion, give rise to repulsive interactions between patch fermions, which favor SDW rather than CDW instabilities. Indeed, the RG phase diagram (Fig. 4) suggests that attraction in the $g_1^{(0)}$ or $g_3^{(0)}$ channels is likely necessary to stabilize CDW order. Here, we show that the electron-optical phonon interaction may renormalize $g_1^{(0)}$ or $g_3^{(0)}$, and lead to attraction in these channels. Specifically, we define $g_i^{(0)} = g_{el,i}^{(0)} + \delta g_i^{(0)}$, where $g_{el,i}^{(0)}$ is the bare interaction due to screened Coulomb repulsion, and compute the renormalization $\delta g_i^{(0)}$.

Consider the standard coupling of electron density with an optical phonon. Because g_1 (g_3) transfers spin (charge) between saddle points, these two interactions cannot be generated from coupling to a zone center phonon. Instead, both $\delta g_1^{(0)}$ and $\delta g_3^{(0)}$ require coupling to a phonon at momentum \mathbf{M} . Conversely, $\delta g_2^{(0)}$ and $\delta g_4^{(0)}$ are generated from coupling with a zone center phonon. A recent *ab initio* calculation and experiment suggest softening of a breathing phonon mode at \mathbf{M} [23,70]. With these considerations in mind, we focus on the coupling with a phonon at \mathbf{M} .

To leading (0th) order in spatial derivatives, the electron-phonon coupling can be expressed as

$$\mathcal{H}_{el-ph} = \sum_{q,k,\Gamma,\alpha} g_{\Gamma} u_{\Gamma,-k}(\mathbf{M}_\alpha) \Psi_{q+k}^\dagger \Lambda_{\Gamma,\alpha} \Psi_q, \quad (\text{B1})$$

where $\alpha = 1, 2, 3$ labels the momentum \mathbf{M}_α , Γ labels the irreducible representation (irrep) of the little group at \mathbf{M}_α . In this notation, $u_\Gamma(\mathbf{M}_\alpha)$ is the optical phonon mode near \mathbf{M}_α in irrep Γ , $\Lambda_{\Gamma,\alpha}$ is obtained such that the fermion bilinear $\Psi_q^\dagger \Lambda_{\Gamma,\alpha} \Psi_q$ transforms as Γ irrep at \mathbf{M}_α . Note that in Eq. (B1), the momentum \mathbf{k} is small, i.e., within the continuum model, and the large momentum transfer \mathbf{M}_α is treated via the flavor indices of the fermion fields.

Without loss of generality, we consider \mathbf{M}_1 , whose little group is $D_{2h} = \langle C_2', C_2'', i \rangle$ (see Fig. 1), where $\langle \dots \rangle$ indicates the group generated by “.” operations. Here, C_2' and C_2'' are twofold rotation along the y and x axis, respectively. i denotes

inversion. Using the transformation of Bloch wave functions,

$$\begin{aligned} \mathcal{U}_O \psi_{n,k}(\mathbf{r}) &= \mathcal{U}_O e^{iq \cdot \mathbf{r}} u_{n,q}(\mathbf{r}) = e^{iq \cdot O\mathbf{r}} u_{n,q}(O\mathbf{r}) \\ &= e^{iO^{-1}q \cdot \mathbf{r}} u_{n,O^{-1}q}(\mathbf{r}) = \psi_{n,O^{-1}q}(\mathbf{r}), \end{aligned} \quad (\text{B2})$$

where $O \in D_{2h}$, we find that the fermion bilinear at momentum \mathbf{M}_1 from the patch fermions should be in either the Γ_1^+ or Γ_3^+ irrep of D_{2h} , with

$$\Lambda_{\Gamma_1^+} = \begin{pmatrix} 0 & 0 & 0 \\ 0 & 0 & 1 \\ 0 & 1 & 0 \end{pmatrix}, \quad \Lambda_{\Gamma_3^+} = \begin{pmatrix} 0 & 0 & 0 \\ 0 & 0 & i \\ 0 & -i & 0 \end{pmatrix}. \quad (\text{B3})$$

Similarly, the representation of optical phonon modes at \mathbf{M}_1 in irrep Γ_1^+, Γ_3^+ can be identified using [76]

$$\Gamma_{\text{oph}} = \Gamma_{\text{equiv}} \times \Gamma_{\text{vec}}, \quad (\text{B4})$$

where Γ_{equiv} is the equivalence representation for the kagome lattice sites at \mathbf{M} , Γ_{vec} is the representation for lattice displacement, the same as that for a 3D vector. The $\Gamma_{\text{oph},1}^+$ irrep comes from either $\Gamma_{\text{equiv},2}^- \times \Gamma_{\text{vec},2}^-$ or $\Gamma_{\text{equiv},4}^- \times \Gamma_{\text{vec},4}^-$ optical phonon modes. While the $\Gamma_{\text{oph},3}^+$ irrep comes from either $\Gamma_{\text{equiv},2}^- \times \Gamma_{\text{vec},4}^-$ or $\Gamma_{\text{equiv},4}^- \times \Gamma_{\text{vec},2}^-$ optical phonon modes. For example, both the “star of David” and the “inverse star of David” breathing phonon mode studied in Ref. [70] comes from the $\Gamma_{\text{oph},1}^+ = \Gamma_{\text{equiv},2}^- \times \Gamma_{\text{vec},2}^-$ optical phonon mode related by reversing the sign of the lattice displacement field.

The effective four-fermion interaction renormalized by \mathcal{H}_{el-ph} reads as

$$\delta \mathcal{H}_{\text{eff}} = \sum_{q,q',\Gamma,\alpha} \mathcal{V}_\Gamma (\Psi_q^\dagger \Lambda_{\Gamma,\alpha} \Psi_{q'}) (\Psi_{q'}^\dagger \Lambda_{\Gamma,\alpha} \Psi_q), \quad (\text{B5})$$

where $\mathcal{V}_\Gamma = g_\Gamma^2 \mathcal{D}_\Gamma(\mathbf{M}_1, \Omega_n = 0) = -\frac{2g_\Gamma^2}{\omega_{\Gamma,\mathbf{M}_1}} < 0$, with $\omega_{\Gamma,\mathbf{k}}$ the phonon spectrum, $\mathcal{D}_\Gamma(\mathbf{k}, \Omega_n) = \frac{2\omega_{\Gamma,\mathbf{k}}}{(i\Omega_n)^2 - \omega_{\Gamma,\mathbf{k}}^2}$ the phonon propagator. This gives finally

$$\begin{aligned} \delta g_1^{(0)} &= \mathcal{V}_{\Gamma_1^+} + \mathcal{V}_{\Gamma_3^+}, \\ \delta g_3^{(0)} &= \mathcal{V}_{\Gamma_1^+} - \mathcal{V}_{\Gamma_3^+}. \end{aligned} \quad (\text{B6})$$

It is straightforward to see that $\delta g_1^{(0)} < 0$ while the sign of $\delta g_3^{(0)}$ depends on the relative strength of $\mathcal{V}_{\Gamma_1^+}$ and $\mathcal{V}_{\Gamma_3^+}$. As a result, all three fixed-point solutions may be approached when the electron-phonon interaction is taken into account.

Experimentally, one may test for the significance of electron-phonon coupling by probing the effect on the phonons. In particular, the coupling \mathcal{H}_{el-ph} also renormalizes the phonon spectrum, and lowers the optical phonon gap. Indeed, the phonon gap for $u_{\Gamma_1^+}, u_{\Gamma_3^+}$ is lowered by $\delta m_{\text{oph}} \sim g_\Gamma^2 \Pi_{\text{ph}}(\mathbf{M})$, which may lead to a Peierls structural transition when the renormalized phonon spectrum becomes gapless at \mathbf{M} .

Does the CDW order observed in the kagome materials come from electronic or structural instabilities? While the full answer to this question requires knowledge of the microscopic details and self-consistent analysis of the electron-phonon coupled system, we note that the four-fermion interaction can be significantly enhanced in the RG flow near the fixed point. Moreover, in the weak coupling limit, as $g_{el,i}^{(0)}$ is weak, a moderate electron-phonon interaction could alter the sign of

the bare fermion interaction, and lead to CDW ordering due to an electronic instability.

APPENDIX C: SOLUTIONS OF THE RCDW MEAN FIELD THEORY

Here, we discuss the possible solutions of the rCDW mean field theory using only general arguments involving symmetry and differential topology. The rCDW free energy which is a function of the three rCDW order parameters, N_1, N_2, N_3 , can be thought of as a function defined on \mathbb{R}^3 spanned by the rCDW vectors $\mathbf{N} = (N_1, N_2, N_3)$. To find the solution of the rCDW mean field theory, we need to find the global minima of the free energy in \mathbb{R}^3 , but, for simplicity, we fix $|\mathbf{N}| = N_0$ where $N_0 > 0$ is an arbitrary value and look for all possible minima of the free energy defined on the sphere S^2 with radius N_0 . This will give us a set of possible directions in which the global minima of the free energy must point.

We begin by identifying all possible stationary points of the rCDW free energy defined on S^2 using symmetry arguments. Starting with the definition of the rCDW order parameters (Table I), it is straightforward to calculate how \mathbf{N} transforms under the microscopic symmetries of the lattice and then to figure out that the free energy must be invariant under symmetry operations of the tetrahedral point group T_d . (The \hat{N}_α axes coincide with the twofold axes of T_d .) From this, we can immediately identify the high-symmetry points on S^2 which must be stationary points of the free energy. These points can be categorized into three classes which we call the 3Q+, 3Q-, and 1Q classes. They are defined as

$$\begin{aligned} 3Q+ &: \{(111), (1\bar{1}\bar{1}), (\bar{1}1\bar{1}), (\bar{1}\bar{1}1)\}, \\ 3Q- &: \{(\bar{1}\bar{1}\bar{1}), (\bar{1}11), (1\bar{1}1), (11\bar{1})\}, \\ 1Q &: \{(100), (010), (001), (\bar{1}00), (0\bar{1}0), (00\bar{1})\}, \end{aligned}$$

where the triplet notation (N_1, N_2, N_3) denotes the directions of the rCDW vectors on S^2 . Each class is an orbit of points generated by T_d . The + and - notations come from the fact that points in the 3Q+ and 3Q- classes satisfy $N_1 N_2 N_3 > 0$ and $N_1 N_2 N_3 < 0$, respectively.

The threefold axes of T_d go through the 3Q \pm points. This tells us that the sign of the curvature at those points must be the same in all directions. Therefore, points in the 3Q \pm classes must be a minima or maxima. On the other hand, we cannot make a similar argument for the points in the 1Q class which coincide with the twofold axes, so the 1Q points can be extrema or saddle points.

In addition to the 3Q \pm and 1Q points, there may be other stationary points which are not necessarily guaranteed by symmetry. We can categorize these low-symmetry points using the Wyckoff positions c, d of T_d which have multiplicities $n_c = 12, n_d = 24$, respectively. Like the 1Q class, these points can correspond to either extrema or saddle points of the free energy.

Next, we use a theory from differential topology known as Morse theory to obtain a constraint on the number of extrema

and saddle points of the free energy defined on S^2 . In general, the free energy defined on S^2 is a smooth function, and its Hessian is not singular at stationary points. Such a function is called a Morse function, and according to Morse theory, Morse functions must satisfy

$$n_{\max} + n_{\min} - n_{\text{sp}} = \chi = 2, \quad (\text{C1})$$

where $n_{\max}, n_{\min}, n_{\text{sp}}$ are the total number of maxima, minima, and saddle points, respectively, and $\chi = 2$ is the Euler characteristic of S^2 [77].

Using Eq. (C1), we can enumerate every possible realization of stationary points on S^2 that is permitted by symmetry and topology. First, assume that the 3Q \pm , 1Q classes are the only stationary points on S^2 . Since the 3Q \pm points must be extrema, Eq. (C1) can only be satisfied if the 1Q points are saddle points ($n_{\max} + n_{\min} = 8$ and $n_{\text{sp}} = 6$). Next, assume that there are stationary points at low-symmetry points too. The 1Q points can also be extrema of the free energy if there are saddle points at a Wyckoff position c ($n_{\max} + n_{\min} = 14$ and $n_{\text{sp}} = 12$). For both scenarios the minima of the free energy on S^2 are found only at the 3Q \pm and/or 1Q points. However, it turns out there are actually an infinite number of other ways to satisfy Eq. (C1). For example, Eq. (C1) is trivially satisfied if we assume the extrema are located at the 3Q \pm and 1Q points, a single Wyckoff position c , and m different Wyckoff positions d and the saddle points are located at a separate set of $m + 1$ different Wyckoff positions d ($n_{\max} + n_{\min} = 26 + 24m$ and $n_{\text{sp}} = 24 + 24m$). In these cases, the minima of the free energy can be found anywhere on S^2 , and the global minima of the free energy can point in any direction. However, because of the large multiplicity of the Wyckoff positions c and d , the free energy has a large number of extrema which correspond to a highly oscillatory behavior of the free energy on S^2 . This can only come from high-order terms with large powers of N which, we argue, are not physically relevant at low energies and near the transition temperature in particular. Therefore, given this assumption, the global minima of the rCDW free energy must belong to either the 3Q \pm or 1Q classes.

A similar analysis can be extended to the iCDW and rSDW order parameters. Like the rCDW order parameters, if we calculate how the iCDW and the individual components of the rSDW order parameters transform under the microscopic symmetries of the system, we find that their free energies have a cubic point-group symmetry O_h instead of T_d because they are odd under time-reversal symmetry unlike the rCDW order parameters. In this case, the 3Q \pm classes can be transformed into each other by the symmetries of O_h , so there are only two classes of high-symmetry points: the 3Q and 1Q classes, where the 3Q class is a union of the 3Q \pm classes.

APPENDIX D: LANDAU THEORY COEFFICIENTS

The coefficients K_1, K_2, K_3, K_4 of the Landau theory defined in Eq. (12) are

$$K_1(T, \mu) = \frac{1}{2\Lambda^2} \int_{-\Lambda}^{\Lambda} \frac{d^2q}{(2\pi)^2} \frac{f(\varepsilon_2(\mathbf{q}) - \mu) - f(\varepsilon_3(\mathbf{q}) - \mu)}{\varepsilon_2(\mathbf{q}) - \varepsilon_3(\mathbf{q})}, \quad (\text{D1})$$

$$K_2(T, \mu) = -\frac{1}{2\Lambda^2} \int_{-\Lambda}^{\Lambda} \frac{d^2q}{(2\pi)^2} \left(\frac{f(\varepsilon_1(\mathbf{q}) - \mu)}{[\varepsilon_1(\mathbf{q}) - \varepsilon_2(\mathbf{q})][\varepsilon_1(\mathbf{q}) - \varepsilon_3(\mathbf{q})]} + \frac{f(\varepsilon_2(\mathbf{q}) - \mu)}{[\varepsilon_2(\mathbf{q}) - \varepsilon_1(\mathbf{q})][\varepsilon_2(\mathbf{q}) - \varepsilon_3(\mathbf{q})]} + \frac{f(\varepsilon_3(\mathbf{q}) - \mu)}{[\varepsilon_3(\mathbf{q}) - \varepsilon_1(\mathbf{q})][\varepsilon_3(\mathbf{q}) - \varepsilon_2(\mathbf{q})]} \right), \quad (\text{D2})$$

$$K_3(T, \mu) = \frac{1}{24\Lambda^2} \int_{-\Lambda}^{\Lambda} \frac{d^2q}{(2\pi)^2} \left(\frac{f'(\varepsilon_1(\mathbf{q}) - \mu)}{[\varepsilon_1(\mathbf{q}) - \varepsilon_2(\mathbf{q})][\varepsilon_1(\mathbf{q}) - \varepsilon_3(\mathbf{q})]} + \frac{f'(\varepsilon_2(\mathbf{q}) - \mu)}{[\varepsilon_2(\mathbf{q}) - \varepsilon_1(\mathbf{q})][\varepsilon_2(\mathbf{q}) - \varepsilon_3(\mathbf{q})]} + \frac{f'(\varepsilon_3(\mathbf{q}) - \mu)}{[\varepsilon_3(\mathbf{q}) - \varepsilon_1(\mathbf{q})][\varepsilon_3(\mathbf{q}) - \varepsilon_2(\mathbf{q})]} \right), \quad (\text{D3})$$

$$K_4(T, \mu) = -\frac{1}{8\Lambda^2} \int_{-\Lambda}^{\Lambda} \frac{d^2q}{(2\pi)^2} \left(\frac{f(\varepsilon_2(\mathbf{q}) - \mu) - f(\varepsilon_3(\mathbf{q}) - \mu)}{[\varepsilon_2(\mathbf{q}) - \varepsilon_3(\mathbf{q})]^3} - \frac{f'(\varepsilon_2(\mathbf{q}) - \mu) + f'(\varepsilon_3(\mathbf{q}) - \mu)}{2[\varepsilon_2(\mathbf{q}) - \varepsilon_3(\mathbf{q})]^2} \right), \quad (\text{D4})$$

where $f(\varepsilon) = 1/[\exp(\varepsilon/T) + 1]$ is the Fermi-Dirac function. These integrals can be evaluated asymptotically in the limit $\mu, k_B T \ll a\Lambda^2, b\Lambda^2$. If we assume perfect nesting, the patch dispersions take the form

$$\varepsilon_1(\mathbf{q}) = \frac{3t}{4}(3q_x^2 - q_y^2), \quad (\text{D5})$$

$$\varepsilon_2(\mathbf{q}) = \frac{3t}{4}2q_y(q_y + \sqrt{3}q_x), \quad (\text{D6})$$

$$\varepsilon_3(\mathbf{q}) = \frac{3t}{4}2q_y(q_y - \sqrt{3}q_x), \quad (\text{D7})$$

where $t > 0$. Given this definition, the asymptotic expressions of K_2, K_3, K_4 in the limit $\mu, k_B T \ll t\Lambda^2$ are

$$K_2 \approx -\frac{16}{\pi^2 t \Lambda^2 k_B T} H_2(\mu/k_B T), \quad (\text{D8})$$

$$K_3 \approx \frac{8}{3\pi^2 \Lambda^2 (k_B T)^2} H_3(\mu/k_B T), \quad (\text{D9})$$

$$K_4 \approx \frac{1}{12\sqrt{3}\pi^2 t \Lambda^2 (k_B T)^2} H_4(\mu/k_B T) \ln(t\Lambda^2/k_B T), \quad (\text{D10})$$

where H_2, H_3, H_4 are the integral functions

$$H_2(z) = \int_0^\infty dx \int_0^{x/\sqrt{3}} dy \left(\frac{F(\tilde{\varepsilon}_1(x, y) - z)}{[\tilde{\varepsilon}_1(x, y) - \tilde{\varepsilon}_2(x, y)][\tilde{\varepsilon}_1(x, y) - \tilde{\varepsilon}_3(x, y)]} - \frac{F(\tilde{\varepsilon}_2(x, y) - z)}{[\tilde{\varepsilon}_1(x, y) - \tilde{\varepsilon}_2(x, y)][\tilde{\varepsilon}_2(x, y) - \tilde{\varepsilon}_3(x, y)]} + \frac{F(\tilde{\varepsilon}_3(x, y) - z)}{[\tilde{\varepsilon}_1(x, y) - \tilde{\varepsilon}_3(x, y)][\tilde{\varepsilon}_2(x, y) - \tilde{\varepsilon}_3(x, y)]} \right), \quad (\text{D11})$$

$$H_3(z) = \int_0^\infty dx \int_0^{x/\sqrt{3}} dy \left(\frac{F'(\tilde{\varepsilon}_1(x, y) - z)}{[\tilde{\varepsilon}_1(x, y) - \tilde{\varepsilon}_2(x, y)][\tilde{\varepsilon}_1(x, y) - \tilde{\varepsilon}_3(x, y)]} - \frac{F'(\tilde{\varepsilon}_2(x, y) - z)}{[\tilde{\varepsilon}_1(x, y) - \tilde{\varepsilon}_2(x, y)][\tilde{\varepsilon}_2(x, y) - \tilde{\varepsilon}_3(x, y)]} + \frac{F'(\tilde{\varepsilon}_3(x, y) - z)}{[\tilde{\varepsilon}_1(x, y) - \tilde{\varepsilon}_3(x, y)][\tilde{\varepsilon}_2(x, y) - \tilde{\varepsilon}_3(x, y)]} \right), \quad (\text{D12})$$

$$H_4(z) = \int_0^\infty dv \left(\frac{-F(v - z) + F(-v - z)}{v^3} + \frac{F'(v - z) + F'(-v - z)}{z^2} \right). \quad (\text{D13})$$

In the equations above, $F(x) = 1/(e^x + 1)$, and $\tilde{\varepsilon}_1(x, y) = 3x^2 - y^2$, $\tilde{\varepsilon}_2(x, y) = 2y(y + \sqrt{3}x)$, $\tilde{\varepsilon}_3(x, y) = 2y(y - \sqrt{3}x)$. The expression holds for arbitrary ratios of $\mu/k_B T$. The values of the H_2, H_3, H_4 when $\mu \ll k_B T$ are

$$H_2(0) \approx 0.039\,571, \quad (\text{D14})$$

$$H_3(0) \approx 0.014\,216, \quad (\text{D15})$$

$$H_4(0) \approx 0.213\,139. \quad (\text{D16})$$

H_2, H_3, H_4 each change sign once at the following values:

$$z_{0,2} \approx 2.142\,68, \quad (\text{D17})$$

$$z_{0,3} \approx 4.051\,61, \quad (\text{D18})$$

$$z_{0,4} \approx 1.910\,67. \quad (\text{D19})$$

The expression for K_1 can be evaluated asymptotically when $\mu \ll k_B T$:

$$K_1 \approx -\frac{1}{6\sqrt{3}\pi^2 t \Lambda^2} [\ln(t\Lambda^2/k_B T)^2 + 2 \ln 3 \ln(t\Lambda^2/k_B T)]. \quad (\text{D20})$$

For $\mu \ll T$, $K_3 - 2K_4$ which determines whether the quartic term of the rCDW Landau theory prefers a 3Q+ or 3Q- configuration is

$$K_3 - 2K_4 \approx \frac{1}{\pi^2 t \Lambda^2 (k_B T)^2} \left(\frac{8H_3(0)}{3} - \frac{H_4(0)}{12\sqrt{3}} \ln(t\Lambda^2/k_B T) \right). \quad (\text{D21})$$

Therefore, $K_3 - 2K_4 < 0$ when

$$\frac{\mu}{t\Lambda^2} \ll \frac{k_B T}{t\Lambda^2} < \exp\left(-32\sqrt{3} \frac{H_3(0)}{H_4(0)}\right) \approx 0.0248. \quad (\text{D22})$$

APPENDIX E: DERIVATION OF EQ. (22): THE CURRENT OPERATOR

Here, we show more details to obtain the bond current operator, which is defined from the continuity equation of charge density. If we define the charge density at site \mathbf{r}_α as $\hat{n}_{\mathbf{r}_\alpha} = -e d_{\mathbf{r}_\alpha}^\dagger d_{\mathbf{r}_\alpha}$, the lattice version of the continuity equation reads as

$$\frac{d\hat{n}_{\mathbf{r}_\alpha}}{dt} + \sum_{\mathbf{r}_\alpha \rightarrow \mathbf{r}'_{\alpha'}} \hat{j}_{\mathbf{r}_\alpha \mathbf{r}'_{\alpha'}} = 0. \quad (\text{E1})$$

The expression for \hat{j} can be obtained from the equation of motion of $\hat{n}_{\mathbf{r}_\alpha}$ which reads as

$$\frac{d\hat{n}_{\mathbf{r}_\alpha}}{dt} = -\frac{i}{\hbar} [\hat{n}_{\mathbf{r}_\alpha}, \hat{H}] = -\frac{i}{\hbar} [\hat{n}_{\mathbf{r}_\alpha}, \hat{H}_0] + \dots, \quad (\text{E2})$$

where the ellipsis denotes contribution from $[\hat{n}_{\mathbf{r}_\alpha}, \hat{H}_1]$, which only possibly contribute at $O(\phi^2)$ to the bond current order

parameter $\langle \hat{j} \rangle$. On the other hand, as only odd power in ϕ term breaks time-reversal symmetry, we conclude that \hat{H}_1 should not contribute to the bond current order parameter at the mean field level. Hereafter, only the contribution from \hat{H}_0 is considered. The NN bond order requires NN hopping term in \hat{H}_0 . Noting,

$$\begin{aligned} [\hat{n}_{\mathbf{r}_\alpha}, \hat{H}_0] &= \left[\hat{n}_{\mathbf{r}_\alpha}, t_1 \sum_{(\mathbf{r}'_{\alpha'}, \mathbf{r}'_{\alpha'} + \mathbf{e}_\beta)} d_{\mathbf{r}'_{\alpha'}}^\dagger d_{\mathbf{r}'_{\alpha'} + \mathbf{e}_\beta} + d_{\mathbf{r}'_{\alpha'} + \mathbf{e}_\beta}^\dagger d_{\mathbf{r}'_{\alpha'}} \right] \\ &= \left[\hat{n}_{\mathbf{r}_\alpha}, t_1 \sum_{\alpha \neq \beta} d_{\mathbf{r}_\alpha}^\dagger d_{\mathbf{r}_\alpha + \mathbf{e}_\beta} + d_{\mathbf{r}_\alpha + \mathbf{e}_\beta}^\dagger d_{\mathbf{r}_\alpha} \right] \\ &= -e t_1 \sum_{\alpha \neq \beta} (d_{\mathbf{r}_\alpha}^\dagger d_{\mathbf{r}_\alpha + \mathbf{e}_\beta} - d_{\mathbf{r}_\alpha + \mathbf{e}_\beta}^\dagger d_{\mathbf{r}_\alpha}), \end{aligned} \quad (\text{E3})$$

where the second line comes from the fact that the commutator is nonzero only for bond satisfying $\mathbf{r}_\alpha = \mathbf{r}'_{\alpha'}$ or $\mathbf{r}_\alpha = \mathbf{r}'_{\alpha'} + \mathbf{e}_\beta$, we find Eq. (22) in the main text.

-
- [1] M. Imada, A. Fujimori, and Y. Tokura, Metal-insulator transitions, *Rev. Mod. Phys.* **70**, 1039 (1998).
- [2] J. Ngai, F. Walker, and C. Ahn, Correlated oxide physics and electronics, *Annu. Rev. Mater. Res.* **44**, 1 (2014).
- [3] D. C. Johnston, The puzzle of high temperature superconductivity in layered iron pnictides and chalcogenides, *Adv. Phys.* **59**, 803 (2010).
- [4] D. J. Scalapino, A common thread: The pairing interaction for unconventional superconductors, *Rev. Mod. Phys.* **84**, 1383 (2012).
- [5] M. Sato and Y. Ando, Topological superconductors: A review, *Rep. Prog. Phys.* **80**, 076501 (2017).
- [6] A. W. Tsien, R. Hovden, D. Wang, Y. D. Kim, J. Okamoto, K. A. Spoth, Y. Liu, W. Lu, Y. Sun, J. C. Hone, L. F. Kourkoutis, P. Kim, and A. N. Pasupathy, Structure and control of charge density waves in two-dimensional 1T-TaS₂, *Proc. Natl. Acad. Sci. U.S.A.* **112**, 15054 (2015).
- [7] L. Ye, M. Kang, J. Liu, F. Von Cube, C. R. Wicker, T. Suzuki, C. Jozwiak, A. Bostwick, E. Rotenberg, D. C. Bell *et al.*, Massive dirac fermions in a ferromagnetic kagome metal, *Nature (London)* **555**, 638 (2018).
- [8] I. R. Fisher, L. Degiorgi, and Z. X. Shen, In-plane electronic anisotropy of underdoped “122” Fe-arsenide superconductors revealed by measurements of detwinned single crystals, *Rep. Prog. Phys.* **74**, 124506 (2011).
- [9] Y. Sato, S. Kasahara, H. Murayama, Y. Kasahara, E. G. Moon, T. Nishizaki, T. Loew, J. Porras, B. Keimer, T. Shibauchi, and Y. Matsuda, Thermodynamic evidence for a nematic phase transition at the onset of the pseudogap in YBa₂Cu₃O_y, *Nat. Phys.* **13**, 1074 (2017).
- [10] C. M. Varma, P. B. Littlewood, S. Schmitt-Rink, E. Abrahams, and A. E. Ruckenstein, Phenomenology of the Normal State of Cu-O High-Temperature Superconductors, *Phys. Rev. Lett.* **63**, 1996 (1989).
- [11] G. R. Stewart, Non-Fermi-liquid behavior in *d*- and *f*-electron metals, *Rev. Mod. Phys.* **73**, 797 (2001).
- [12] O. Gunnarsson, M. Calandra, and J. E. Han, Colloquium: Saturation of electrical resistivity, *Rev. Mod. Phys.* **75**, 1085 (2003).
- [13] C. M. Varma, Colloquium: Linear in temperature resistivity and associated mysteries including high temperature superconductivity, *Rev. Mod. Phys.* **92**, 031001 (2020).
- [14] A. Chubukov, Pairing mechanism in Fe-based superconductors, *Annu. Rev. Condens. Matter Phys.* **3**, 57 (2012).
- [15] Q. Si, R. Yu, and E. Abrahams, High-temperature superconductivity in iron pnictides and chalcogenides, *Nat. Rev. Mater.* **1**, 16017 (2016).
- [16] K. Takada, H. Sakurai, E. Takayama-Muromachi, F. Izumi, R. A. Dilanian, and T. Sasaki, Superconductivity in two-dimensional CoO₂ layers, *Nature (London)* **422**, 53 (2003).
- [17] M. L. Foo, Y. Wang, S. Watauchi, H. W. Zandbergen, T. He, R. J. Cava, and N. P. Ong, Charge Ordering, Commensurability, and Metallicity in the Phase Diagram of the Layered Na_xCoO₂, *Phys. Rev. Lett.* **92**, 247001 (2004).
- [18] J. D. Jorgensen, M. Avdeev, D. G. Hinks, J. C. Burley, and S. Short, Crystal structure of the sodium cobaltate deuterate superconductor Na_xCoO₂ · 4xD₂O ($x \approx \frac{1}{3}$), *Phys. Rev. B* **68**, 214517 (2003).
- [19] B. R. Ortiz, L. C. Gomes, J. R. Morey, M. Winiarski, M. Bordelon, J. S. Mangum, I. W. H. Oswald, J. A. Rodriguez-Rivera, J. R. Neilson, S. D. Wilson, E. Ertekin, T. M. McQueen, and E. S. Toberer, New kagome prototype materials: discovery of KV₃Sb₅, RbV₃Sb₅, and CsV₃Sb₅, *Phys. Rev. Mater.* **3**, 094407 (2019).
- [20] Y. X. Jiang, J. X. Yin, M. M. Denner, N. Shumiya, B. R. Ortiz, J. He, X. Liu, S. S. Zhang, G. Chang, I. Belopolski, Q. Zhang, M. S. Hossain, T. A. Cochran, D. Multer, M. Litskevich, Z.-J. Cheng, X. P. Yang, Z. Guguchia, G. Xu, Z. Wang *et al.*, Unconventional chiral charge order in kagome superconductor KV₃Sb₅, *Nat. Mater.* (2021), doi: 10.1038/s41563-021-01034-y.
- [21] H. Zhao, H. Li, B. R. Ortiz, S. M. L. Teicher, T. Park, M. Ye, Z. Wang, L. Balents, S. D. Wilson, and I. Zeljkovic,

- Cascade of correlated electron states in a kagome superconductor CsV₃Sb₅, [arXiv:2103.03118](#).
- [22] H. X. Li, T. T. Zhang, Y. Y. Pai, C. Marvinney, A. Said, T. Yilmaz, Q. Yin, C. Gong, Z. Tu, E. Vescovo, R. G. Moore, S. Murakami, H. C. Lei, H. N. Lee, B. Lawrie, and H. Miao, Observation of Unconventional Charge Density Wave without Acoustic Phonon Anomaly in Kagome Superconductors AV₃Sb₅ (A=Rb,Cs), [arXiv:2103.09769](#).
- [23] E. Uykur, B. R. Ortiz, S. D. Wilson, M. Dressel, and A. A. Tsirlin, Optical detection of charge-density-wave instability in the non-magnetic kagome metal KV₃Sb₅, [arXiv:2103.07912](#).
- [24] Z. Liang, X. Hou, W. Ma, F. Zhang, P. Wu, Z. Zhang, F. Yu, J. J. Ying, K. Jiang, L. Shan, Z. Wang, and X. H. Chen, Three-dimensional charge density wave and robust zero-bias conductance peak inside the superconducting vortex core of a kagome superconductor CsV₃Sb₅, [arXiv:2103.04760](#).
- [25] X. Zhou, Y. Li, X. Fan, J. Hao, Y. Dai, Z. Wang, Y. Yao, and H.-H. Wen, Origin of the Charge Density Wave in the Kagome Metal CsV₃Sb₅ as Revealed by Optical Spectroscopy, *Phys. Rev. B* **104**, L041101 (2021).
- [26] E. M. Kenney, B. R. Ortiz, C. Wang, S. D. Wilson, and M. Graf, Absence of local moments in the kagome metal KV₃Sb₅ as determined by muon spin spectroscopy, *J. Phys.: Condens. Matter* **33**, 235801 (2021).
- [27] B. R. Ortiz, S. M. L. Teicher, L. Kautzsch, P. M. Sarte, J. P. C. Ruff, R. Seshadri, and S. D. Wilson, Fermi surface mapping and the nature of charge density wave order in the kagome superconductor CsV₃Sb₅, [arXiv:2104.07230](#).
- [28] B. R. Ortiz, P. M. Sarte, E. M. Kenney, M. J. Graf, S. M. L. Teicher, R. Seshadri, and S. D. Wilson, Superconductivity in the z₂ kagome metal KV₃Sb₅, *Phys. Rev. Mater.* **5**, 034801 (2021).
- [29] C. C. Zhao, L. S. Wang, W. Xia, Q. W. Yin, J. M. Ni, Y. Y. Huang, C. P. Tu, Z. C. Tao, Z. J. Tu, C. S. Gong, H. C. Lei, Y. F. Guo, X. F. Yang, and S. Y. Li, Nodal superconductivity and superconducting domes in the topological Kagome metal CsV₃Sb₅, [arXiv:2102.08356](#).
- [30] K. Y. Chen, N. N. Wang, Q. W. Yin, Z. J. Tu, C. S. Gong, J. P. Sun, H. C. Lei, Y. Uwatoko, and J. G. Cheng, Double superconducting dome and triple enhancement of T_c in the kagome superconductor CsV₃Sb₅ under high pressure, *Phys. Rev. Lett.* **126**, 247001 (2021).
- [31] H. Chen, H. Yang, B. Hu, Z. Zhao, J. Yuan, Y. Xing, G. Qian, Z. Huang, G. Li, Y. Ye, Q. Yin, C. Gong, Z. Tu, H. Lei, S. Ma, H. Zhang, S. Ni, H. Tan, C. Shen, X. Dong, et al., Roton pair density wave and unconventional strong-coupling superconductivity in a topological kagome metal, [arXiv:2103.09188](#).
- [32] W. Duan, Z. Nie, S. Luo, F. Yu, B. R. Ortiz, L. Yin, H. Su, F. Du, A. Wang, Y. Chen, X. Lu, J. Ying, S. D. Wilson, X. Chen, Y. Song, and H. Yuan, Nodeless superconductivity in the kagome metal CsV₃Sb₅, [arXiv:2103.11796](#).
- [33] Z. Zhang, Z. Chen, Y. Zhou, Y. Yuan, S. Wang, L. Zhang, X. Zhu, Y. Zhou, X. Chen, J. Zhou, and Z. Yang, Pressure-induced Reemergence of Superconductivity in Topological Kagome Metal CsV₃Sb₅, *Phys. Rev. B* **103**, 224513 (2021).
- [34] C. Mu, Q. Yin, Z. Tu, C. Gong, H. Lei, Z. Li, and J. Luo, S-wave superconductivity in kagome metal CsV₃Sb₅ revealed by ^{121/123}Sb NQR and ⁵¹V NMR measurements, *Chin. Phys. Lett.* **38**, 077402 (2021).
- [35] S. Ni, S. Ma, Y. Zhang, J. Yuan, H. Yang, Z. Lu, N. Wang, J. Sun, Z. Zhao, D. Li, S. Liu, H. Zhang, H. Chen, K. Jin, J. Cheng, L. Yu, F. Zhou, X. Dong, J. Hu, H.-J. Gao *et al.*, Anisotropic superconducting properties of Kagome metal CsV₃Sb₅, *Chin. Phys. Lett.* **38**, 057403 (2021).
- [36] Y. Xiang, Q. Li, Y. Li, W. Xie, H. Yang, Z. Wang, Y. Yao, and H.-H. Wen, Nematic electronic state and twofold symmetry of superconductivity in the topological kagome metal CsV₃Sb₅, [arXiv:2104.06909](#).
- [37] Q. Wang, Q. Yin, and H. Lei, Giant topological Hall effect of ferromagnetic kagome metal Fe₃Sn₂, *Chin. Phys. B* **29**, 017101 (2020).
- [38] F. H. Yu, T. Wu, Z. Y. Wang, B. Lei, W. Z. Zhuo, J. J. Ying, and X. H. Chen, Concurrence of anomalous Hall effect and charge density wave in a superconducting topological kagome metal, *Phys. Rev. B* **104**, L041103 (2021).
- [39] B. R. Ortiz, S. M. L. Teicher, Y. Hu, J. L. Zuo, P. M. Sarte, E. C. Schueller, A. M. Milinda Abeykoon, M. J. Krogstad, S. Rosenkranz, R. Osborn, R. Seshadri, L. Balents, J. He, and S. D. Wilson, C_{sv3sb5}: A Z₂ topological Kagome Metal with a Superconducting Ground State, *Phys. Rev. Lett.* **125**, 247002 (2020).
- [40] J. Zhao, W. Wu, Y. Wang, and S. A. Yang, Electronic correlations in the normal state of kagome superconductor KV₃Sb₅, *Phys. Rev. B* **103**, L241117 (2021).
- [41] Z. Liu, N. Zhao, Q. Yin, C. Gong, Z. Tu, M. Li, W. Song, Z. Liu, D. Shen, Y. Huang, K. Liu, H. Lei, and S. Wang, Temperature-induced band renormalization and Lifshitz transition in a kagome superconductor RbV₃Sb₅, [arXiv:2104.01125](#).
- [42] Z. Wang, S. Ma, Y. Zhang, H. Yang, Z. Zhao, Y. Ou, Y. Zhu, S. Ni, Z. Lu, H. Chen, K. Jiang, L. Yu, Y. Zhang, X. Dong, J. Hu, H.-J. Gao, and Z. Zhao, Distinctive momentum dependent charge-density-wave gap observed in CsV₃Sb₅ superconductor with topological kagome lattice, [arXiv:2104.05556](#).
- [43] J. E. Hirsch and D. J. Scalapino, Enhanced Superconductivity in Quasi Two-Dimensional Systems, *Phys. Rev. Lett.* **56**, 2732 (1986).
- [44] R. Markiewicz, A survey of the Van Hove scenario for high- T_c superconductivity with special emphasis on pseudogaps and striped phases, *J. Phys. Chem. Solids* **58**, 1179 (1997).
- [45] K. L. Hur and T. Maurice Rice, Superconductivity close to the mott state: From condensed-matter systems to superfluidity in optical lattices, *Ann. Phys.* **324**, 1452 (2009), July 2009 Special Issue.
- [46] R. Nandkishore, L. Levitov, and A. Chubukov, Chiral superconductivity from repulsive interactions in doped graphene, *Nat. Phys.* **8**, 158 (2012).
- [47] R. Nandkishore, G.-W. Chern, and A. V. Chubukov, Itinerant Half-Metal Spin-Density-Wave State on the Hexagonal Lattice, *Phys. Rev. Lett.* **108**, 227204 (2012).
- [48] R. Nandkishore and A. V. Chubukov, Interplay of superconductivity and spin-density-wave order in doped graphene, *Phys. Rev. B* **86**, 115426 (2012).
- [49] Y.-P. Lin and R. M. Nandkishore, Chiral twist on the high- T_c phase diagram in moiré heterostructures, *Phys. Rev. B* **100**, 085136 (2019).
- [50] D. V. Chichinadze, L. Classen, and A. V. Chubukov, Nematic superconductivity in twisted bilayer graphene, *Phys. Rev. B* **101**, 224513 (2020).
- [51] D. V. Chichinadze, L. Classen, and A. V. Chubukov, Valley magnetism, nematicity, and density wave orders in twisted bilayer graphene, *Phys. Rev. B* **102**, 125120 (2020).

- [52] L. Classen, A. V. Chubukov, C. Honerkamp, and M. M. Scherer, Competing orders at higher-order van hove points, *Phys. Rev. B* **102**, 125141 (2020).
- [53] Y.-P. Lin and R. M. Nandkishore, Parquet renormalization group analysis of weak-coupling instabilities with multiple high-order Van Hove points inside the Brillouin zone, *Phys. Rev. B* **102**, 245122 (2020).
- [54] A. T. Zheleznyak, V. M. Yakovenko, and I. E. Dzyaloshinskii, Parquet solution for a flat Fermi surface, *Phys. Rev. B* **55**, 3200 (1997).
- [55] W. Metzner, C. Castellani, and C. D. Castro, Fermi systems with strong forward scattering, *Adv. Phys.* **47**, 317 (1998).
- [56] A. V. Chubukov, D. V. Efremov, and I. Eremin, Magnetism, superconductivity, and pairing symmetry in iron-based superconductors, *Phys. Rev. B* **78**, 134512 (2008).
- [57] A. Chubukov, Renormalization group analysis of competing orders and the pairing symmetry in Fe-based superconductors, *Phys. C (Amsterdam)* **469**, 640 (2009).
- [58] S. M. Teicher (private communication).
- [59] G. F. Koster, *Properties of the Thirty-two Point Groups* (MIT Press, Cambridge, MA, 1963).
- [60] N. Furukawa, T. M. Rice, and M. Salmhofer, Truncation of a Two-Dimensional Fermi Surface due to Quasiparticle Gap Formation at the Saddle Points, *Phys. Rev. Lett.* **81**, 3195 (1998).
- [61] H.-H. Lin, L. Balents, and M. P. A. Fisher, N -chain Hubbard model in weak coupling, *Phys. Rev. B* **56**, 6569 (1997).
- [62] L. Balents and M. P. A. Fisher, Weak-coupling phase diagram of the two-chain Hubbard model, *Phys. Rev. B* **53**, 12133 (1996).
- [63] J. L. Cardy, M. Nauenberg, and D. J. Scalapino, Scaling theory of the Potts-model multicritical point, *Phys. Rev. B* **22**, 2560 (1980).
- [64] M. Schick, Application of the Heisenberg model with cubic anisotropy to phase transitions on surfaces, *Surf. Sci.* **125**, 94 (1983).
- [65] J. M. Carmona, A. Pelissetto, and E. Vicari, N -component Ginzburg-Landau Hamiltonian with cubic anisotropy: A six-loop study, *Phys. Rev. B* **61**, 15136 (2000).
- [66] J. D. Jackson, *Classical Electrodynamics*, 2nd ed. (Wiley, New York, 1999).
- [67] S. Lederer and S. A. Kivelson, Observable nmr signal from circulating current order in YBCO, *Phys. Rev. B* **85**, 155130 (2012).
- [68] M. Klug, J. Kang, R. M. Fernandes, and J. Schmalian, Orbital loop currents in iron-based superconductors, *Phys. Rev. B* **97**, 155130 (2018).
- [69] J. Shi, G. Vignale, D. Xiao, and Q. Niu, Quantum Theory of Orbital Magnetization and its Generalization to Interacting Systems, *Phys. Rev. Lett.* **99**, 197202 (2007).
- [70] H. Tan, Y. Liu, Z. Wang, and B. Yan, Charge density waves and electronic properties of superconducting kagome metals, [arXiv:2103.06325](https://arxiv.org/abs/2103.06325).
- [71] H. Li, H. Zhao, B. R. Ortiz, T. Park, M. Ye, L. Balents, Z. Wang, S. D. Wilson, and I. Zeljkovic (unpublished).
- [72] S.-Y. Yang, Y. Wang, B. R. Ortiz, D. Liu, J. Gayles, E. Derunova, R. Gonzalez-Hernandez, L. Smejkal, Y. Chen, S. S. Parkin *et al.*, Giant, unconventional anomalous Hall effect in the metallic frustrated magnet candidate, KV_3Sb_5 , *Sci. Adv.* **6**, eabb6003 (2020).
- [73] X. Feng, K. Jiang, Z. Wang, and J. Hu, Chiral flux phase in the kagome superconductor AV_3Sb_5 , *Sci. Bull.* (2021), doi: 10.1016/j.scib.2021.04.043.
- [74] M. M. Denner, R. Thomale, and T. Neupert, Analysis of charge order in the kagome metal AV_3Sb_5 ($A = K, Rb, Cs$), [arXiv:2103.14045](https://arxiv.org/abs/2103.14045).
- [75] Y.-P. Lin and R. M. Nandkishore, Complex charge density waves at Van Hove singularity on hexagonal lattices: Haldane-model phase diagram and potential realization in kagome metals AV_3Sb_5 ($A = K, Rb, Cs$), *Phys. Rev. B* **104**, 045122 (2021).
- [76] Dresselhaus, Mildred S. and Dresselhaus, Gene, Jorio, Ado, *Group Theory: Application to the Physics of Condensed Matter* (Springer, Berlin, 2008).
- [77] J. W. Milnor, *Morse Theory*, 5th ed., Annals of Mathematics Studies No. 51 (Princeton University Press, Princeton, NJ, 1973).